Spectroscopic properties and configuration interaction assisted crystal field analysis of Nd^{3+} in neat $Cs_2NaNdCl_6$

Xianju Zhou, Chris S. K. Mak, and Peter A. Tanner
Department of Biology and Chemistry, City University of Hong Kong, Tat Chee Avenue, Kowloon, Hong Kong S.A.R., People's Republic of China

Michèle D. Faucher
88 Avenue Jean Jaurès, 92140 Clamart, France

(Received 16 July 2005; revised manuscript received 13 December 2005; published 21 February 2006)

This paper focuses upon the luminescence and absorption optical properties of trivalent neodymium ions in the neat hexachloroelpasolite $Cs_2NaNdCl_6$, and the crystal field analysis of the resulting dataset. The luminescence investigation spans the spectral region from 7950 to 27800 cm^{-1}, wherein four metastable emitting states $^4F_{3/2}$, $^4F_{5/2}$, $^4G_{7/2}$, and $^4D_{3/2}$ occur, as well as $^2P_{3/2}$ in $Cs_2NaYCl_6:Nd^{3+}$. The zero phonon lines as well as vibronic sidebands in the transitions from these luminescent states to lower terminal terms have been assigned in detail. In particular, for the highest emitting state $^4D_{3/2}$ in $Cs_2NaNdCl_6$ all the transitions to terminal crystal levels with energies below 17 000 cm^{-1} have been assigned. The high resolution absorption spectrum of $Cs_2NaNdCl_6$ has been recorded and analyzed in the range from 400 to 40 000 cm^{-1}, spanning 34 terminal multiplet manifolds. The comparison with the spectra of $Cs_2NaMCl_6:Nd^{3+}$ (M=Gd, Y) is included. The experimental dataset encompasses all 109 crystal field energy levels below 40 000 cm^{-1}, comprising 86 firmly assigned levels and a further 12 tentative ones, i.e., from the total 364 states of f^3, 300 of the first 332 states have been assigned or tentatively assigned. It has been analyzed by the conventional f^3 model as well as by a model which includes configuration interaction with an equiparity p-electron configuration. The f^2p model provides a superior fit than the f^3 model, with overall standard deviations of 12.9 and 32.2 cm^{-1}, respectively for 98 levels. The nature of the latter configuration is discussed and rationalized with reference to previous analyses for Pr^{3+}, Er^{3+}, and Tm^{3+}. A comparison is made with other energy level fittings for solid-state Nd^{3+} compounds.

DOI: 10.1103/PhysRevB.73.075113 PACS number(s): 78.40.Ha, 33.20.Lg, 71.70.Ch, 33.50.Dq

I. INTRODUCTION

The energy levels and optical properties of Nd^{3+} in various host lattices have received considerable attention.[1–15] The $4f^3$ *SLJ* energy levels are depicted in Fig. 1. Several studies have focused upon Nd^{3+} in the high site symmetry environment in hexachloroelpasolite hosts, $Cs_2NaLnCl_6:Nd^{3+}$ (Ln=lanthanide ion) which crystallize in the space group $O_h^5(Fm3m)$. In this structure each Ln^{3+} ion is hexa-coordinated to six Cl^- ions and is located at a site of octahedral symmetry in the crystal lattice. The second coordination sphere about each Ln^{3+} ions is comprised of eight Cs^+ ions situated at the vertices of a regular cube, and the third coordination sphere is comprised of six Na^+ ions occupying the vertices of a regular octahedron.[16] Foster *et al.* published the optical spectra and crystal field analysis of Nd^{3+} in the cubic Cs_2NaYCl_6 host.[17] Emission was assigned from several excited states: $^4G_{7/2}$ (in the region from 14 220 to 18 860 cm^{-1}); $^4D_{3/2}$ (in the region from 13 333 to 17 857 cm^{-1}); and the $^2K_{13/2}$ multiplet (from 17 600 to 18 860 cm^{-1}). The latter lines were subsequently shown to be due to Er^{3+} impurity.[18] The excitation spectra and luminescence from the $^4F_{3/2}$ level (at 11 334 cm^{-1}) were studied for Nd^{3+} in the cubic $Cs_2NaGdCl_6$ host,[19] with additional data from the visible electronic absorption spectra being incorporated into an energy level parametrization.[20] The study of the quenching of $^4F_{3/2}$ emission from Nd^{3+} in neat $Cs_2NaNdCl_6$ and several other elpasolite hosts was the focus of two other works.[21,22] More recently, the investigation of the Nd^{3+} $4f^25d$ states in $Cs_2NaNdCl_6$ has been made using ground and excited state absorption. No luminescence is observed from the $4f^25d$ states because nonradiative relaxation occurs from the lowest of the states to the ladder of $4f^3$ levels below.[23]

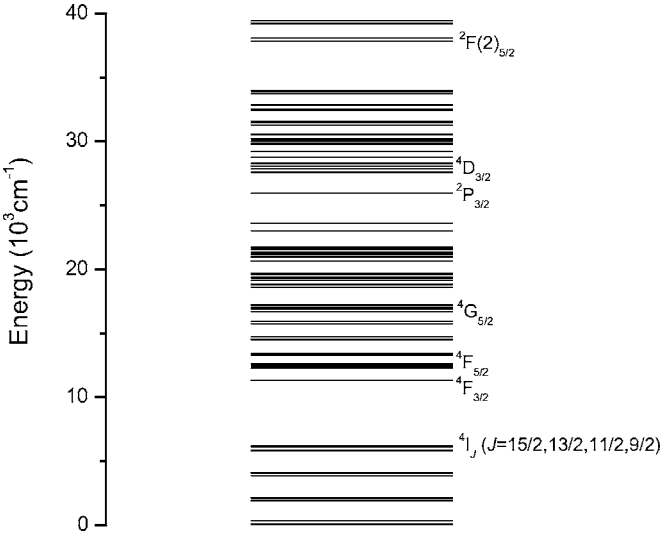

FIG. 1. Energy levels of Nd^{3+} in $Cs_2NaNdCl_6$.

TABLE I. Vibrational structure (in cm^{-1}) in the electronic spectra of $Cs_2NaNdCl_6$ and $Cs_2NaLnCl_6:Nd^{3+}$ at 10–20 K. (Refer to the unit cell group notation in Ref. 25). The multiple structures for each vibrational mode are due to the effects of dispersion and transverse-longitudinal mode splittings (Ref. 24). The relative intensities are an approximate average guide: m, medium; s, strong; w, weak, sh, shoulder. transl., translation; str., stretch; b, bend; ZB, zone boundary.

Unit cell group mode and symmetry	Moiety mode	Displacement energy (cm^{-1}) from electronic origin and relative intensity		
		$Cs_2NaNdCl_6$	$Cs_2NaYCl_6:Nd^{3+}$	$Cs_2NaGdCl_6:Nd^{3+}$
$S_5\tau_{2g}$ Cs^+ lattice		37 m	37 m, 44 m	35 m, 41 m
$S_6\tau_{1u}$ Nd-Cl str.	ν_3	238 m, 249 s 276 mw	246 sh, 261 s, 300 vw	240 m, 256 s, 285 mw
$S_7\tau_{1u}$ Cl-Nd-Cl b.	ν_4	98 s, 120 w	100 s, 116 w, 137 vw	96 s, 122 m
$S_8\tau_{1u}$ Na-Cl str.		176 m	192 m	181 m
$S_9\tau_{1u}$ Cs^+ transl.		60 mw	58 mw	57 sh
$S_{10}\tau_{2u}$ Cl-Nd-Cl b.	ν_6	75 w, 81 s	69 s, 80 sh	68 sh, 77 s

The spectra of Ln^{3+} in elpasolite hosts have recently been reviewed.[24] Pure electronic transitions are electric-dipole (ED) forbidden, but subject to certain selection rules (which are less restrictive for odd-electron systems)[24] and may be magnetic dipole (MD) and/or electric quadrupole (EQ) allowed. Based upon the electronic origins, one-phonon vibronic sidebands are observed with the odd-parity vibrational modes being prominent. The notation and energies of the normal modes for the $Cs_2NaNdCl_6$ system are given in Table I. Although the electronic spectra turn out to be very complex the vibronic fingerprints serve to securely identify the locations of the electronic origins. The study of different transitions originating from and terminating upon the same multiplet term also helps to confirm spectral assignments. The spectra of $Cs_2NaNdCl_6$ are however, more complicated because the crystal undergoes a phase transition at 137 K to the $I4/m\text{-}C_{4h}{}^5$ space group,[26–28] so that the removal of electronic and vibronic high degeneracies results in the splittings of spectral features. Fortunately, the splittings of electronic energy levels are only a few cm^{-1} so that it is a reasonable approximation to model the system as cubic. This is particularly useful since then the derived model parameters can be more meaningfully compared with those for other *neat* $Cs_2NaLnCl_6$ systems rather than with the systems where Nd^{3+} is diluted into transparent cubic elpasolite hosts.

There are several aims of the present study. First, a thorough investigation and rationalization of the intraconfigurational electronic spectra of Nd^{3+} in $Cs_2NaNdCl_6$ has been undertaken. The comparison with $Cs_2NaLnCl_6:Nd^{3+}$ (Ln=Y,Gd) has also been included in order to show that the results are representative and consistent. In particular, the ultraviolet and visible luminescence from the $^4D_{3/2}$ term has been studied and assigned in detail. It is essential that the derived energy level dataset for Nd^{3+} is reasonably complete and moreover, secure and contains no spurious experimental assignments, in order to obtain valid conclusions from the crystal field analysis. In most cases from the present experimental results which utilize cubic, polycrystalline materials, we are unable to assign symmetry representations to the derived crystal field energy levels. However the criterion of completeness is fairly well satisfied so that a valid 1:1 energy level mapping of experiment and theory was possible. The completeness requires that *all* spectral features are reliably assigned and this is the present case except for a few impurity bands which vary in intensity from one sample to another. Thus, the energy level dataset has been analyzed by the conventional $4f^3$ energy level parametrization as well as by the configuration interaction assisted crystal field (CI-ACF) calculation. The previous result for $Cs_2NaPrCl_6$ using the latter model lowered the standard deviation in the energy level fit by a factor of 2.9 from that of the $4f^2$ energy level fit, by including the interaction with the $4fnp$ configuration, where n was assumed to be 6.[29] By contrast, the fits for $Cs_2NaLnCl_6$ [Ln=Er (Ref. 30) and Tm (Ref. 31)] were dramatically improved by including the interaction with the chloride ligand to metal charge-transfer configuration $4f^{N+1}3p^5$. It was therefore intriguing to ascertain how the Nd^{3+} energy level fit would perform by the inclusion of configuration interaction and it is subsequently shown that the energy level fit is improved by a factor of 2.5. In particular, the behaviour of *anomalous* multiplets such as $^2H(2)$ is of interest.

Section II briefly reviews the experimental details. The electronic absorption spectra and emission spectra are presented in Secs. III and IV, respectively. Since hundreds of bands are observed the detailed tabulations have not been included herein but the major assignments are summarized in the figures. The energy level fits and the comparison with other systems are presented in Secs. V to VII. Finally, the major conclusions are given in point form in Sec. VIII.

II. EXPERIMENT

$Cs_2NaNdCl_6$ was prepared from Nd_2O_3 (Strem Chemicals, 99.9%; Berkshire Ores, 99.99%) according to Morss method E.[32] Crystals were grown in vacuum-sealed quartz ampoules which were passed through a Bridgmann furnace at 850 °C. $Cs_2NaYCl_6:Nd^{3+}$ was similarly prepared at 3 at. % and 10 at. % doping levels using Y_2O_3 (Strem, 99.999%), as well as $Cs_2NaGdCl_6:Nd^{3+}$ at 7 at. % doping level (Gd_2O_3 from Strem, 99.99%). Electronic absorption spectra were obtained at resolution 2 cm^{-1}, by a Biorad FTS-60A spectrometer, equipped with DTGS, PbSe, Si and photomultiplier detectors, in the region of 1000 up to 28 000 cm^{-1}. The ultraviolet spectra (up to 40 000 cm^{-1}) were recorded as single-beam spectra at a resolution of between 2–4 cm^{-1} by an Acton 0.5 m monochromator, having an 1800 groove/mm grating blazed at 250 nm, and a back-illuminated SpectruMM CCD detector, using a deuterium (D_2) or a xenon (Xe) lamp as the external light source. All the spectra were recorded between 300 and 10 K with the polished polycrystalline sample housed in an Oxford Instruments closed cycle cryostat. Wavenumber calibrations to vacuum wavelengths were made by standard lamps.

High resolution emission spectra were recorded at temperatures down to 10 K, using a tunable pulsed laser (Panther OPO system pumped by the third harmonic of a Surelite Nd:YAG). The signal was collected at 90° with the Acton 0.5 m monochromator, with gratings blazed at 250 nm (1800 grooves/mm), 500 nm (1200 groove/mm), and 750 nm (600 groove/mm) respectively, and a back-illuminated SpectruMM CCD detector.

III. ELECTRONIC ABSORPTION SPECTRA OF $Cs_2NaNdCl_6$

High resolution absorption spectra for $Cs_2NaNdCl_6$ in the range from 1000 to 40 000 cm^{-1} were recorded and interpreted at various temperatures and although the 30 K spectra served to confirm hot band assignments we mainly limit the discussion to the 10 K spectra. The electronic ground state of the $4f^3$ Nd^{3+} ion is $^4I_{9/2}\, a\Gamma_8$. The excited Γ_6(97 cm^{-1}) and $b\Gamma_8$(338 cm^{-1}) crystal field levels have been assigned from electronic Raman spectra.[33] A splitting of 2.5 ± 0.5 cm^{-1} was often resolved in the absorption spectra for bands corresponding to electronic transitions from the $a\Gamma_8$ quartet state. This is attributed to the ground quartet state splitting into two Kramers doublets since the *neat* Nd^{3+} elpasolite crystal is not cubic below 137 K. In these cases the mean values for the electronic transitions have been listed in Table II and these are underlined. Altogether 86 firmly assigned crystal field levels up to ~40 000 cm^{-1} plus 12 tentative ones, spanning 34 multiplet terms were recorded and analyzed in the present study. Many crystal field states are of very mixed $^{2S+1}L_J$ parentage [for example, Γ_8 at 17 265 cm^{-1}: $^4G_{5/2}$ and $^2G_{7/2}$; Γ_8 at 21 014 cm^{-1}: $^2D(1)_{3/2}$ and $^2P_{3/2}$] but only the principal multiplet term is listed throughout this work.

The low temperature absorption spectra of $Cs_2NaNdCl_6$ are shown in Figs. 2(a)–2(p). The vibronic structures in the figures are labeled according to the unit cell group notation. The moiety modes ν_3, ν_4, and ν_6 correspond to S_6, S_7, and S_{10}, respectively (Table I). All bands have been assigned but for clarity only the stronger features are labeled, as referred to in the text. Even so, it is appreciated that the reader may have considerable difficulty in following the spectra since the detailed structure is not clear and is recorded from only one of the different crystal thicknesses employed. However in view of the large numbers of bands a complete tabulation is not presented. The expanded figures are available as an auxiliary publication.[34] Since band intensities are not relevant in the present study, some parts of Figs. 2(a)–2(p) are scale-expanded for clarity. The main aims of the figures are to show (i) the spectra are much more complex and extensive than those for Nd^{3+} at a noncentrosymmetric site; (ii) that most of the spectral intensity is vibronic in nature; and (iii) to present an archival record of our assignments. The liquid-nitrogen temperature spectra are not useful in most cases (except for the location of S_{10} or S_7 hot bands) because features are blurred and the transitions from the first excited state of $^4I_{9/2}$ (at 97 cm^{-1}) are seldom resolved. The low temperature spectra were recorded for crystals of different thickness which were from different preparations. Some variable-intensity features (labeled "var" in Fig. 2) were identified from one spectrum to another and probably correspond to hydrolysis products and are not further discussed. The spectra recorded in the ultraviolet region were single-beam.

A. Transitions to $^4I_J(J=11/2,13/2,15/2)$

Figure 2(a) shows the room temperature and 77 K absorption spectrum of the transition from the ground state to the first excited multiplet term $^4I_{11/2}$, which comprises four crystal field levels calculated in the order of energy: $a\Gamma_8<\Gamma_7<b\Gamma_8<\Gamma_6$. This transition is unique because most of the intensity arises from the MD mechanism since the free ion selection rules $\Delta S=0$, $\Delta L=0$, and $\Delta J\leqslant 1$ are obeyed. The relative intensities of the four zero phonon lines (ZPL) (at 1921, 1926, 2122, and 2142 cm^{-1}) corresponding to the transitions from $a\Gamma_8$ to the terminal crystal field states of $^4I_{11/2}$ are as expected from the calculation. Since the $\Gamma_6\rightarrow\Gamma_7$ transition is MD forbidden only one hot band is observed for $\Gamma_6\rightarrow a\Gamma_8,\Gamma_7$ (at 1824 cm^{-1}).

The next multiplet term is $^4I_{13/2}$ near 4000 cm^{-1}. The origins of the $a\Gamma_8\rightarrow a\Gamma_7$ and $a\Gamma_8\rightarrow a\Gamma_8$ transitions are weak, sharp bands but there are water bands in this region (not shown in Fig. 2). The ZPL and some of the vibronic structure for the transitions terminating upon $b\Gamma_7$, $b\Gamma_8$, and Γ_6 are marked in Fig. 2(b). The transition to $^4I_{15/2}$ extends from 5797 cm^{-1} to 6491 cm^{-1}, Fig. 2(c) and the intensity is mostly vibronic.

B. Transitions to $^4F_J(J=3/2,5/2,7/2,9/2)$, $^4S_{3/2}$, $^2H(2)_{9/2}$, and $^2H(2)_{11/2}$

Figure 2(d) shows the absorption transition to $^4F_{3/2}$ in $Cs_2NaNdCl_6$ and is in agreement with the spectrum of Tofield and Weber[21] except for a calibration difference of ~10 cm^{-1}. The next group of bands, Fig. 2(e), corresponds to transitions to the multiplet term, $^4F_{5/2}$ which comprises two crystal field levels, Γ_7 and Γ_8. However the transition to

TABLE II. Derived energy levels (in cm^{-1}) of Nd^{3+} in elpasolite hosts.[a]

			$Cs_2NaNdCl_6$		$Cs_2NaYCl_6:Nd^{3+a}$		$Cs_2NaGdCl_6:Nd^{3+a}$		
No.	$^{2S+1}L_J$	IR	Abs.[b]	Em.[c–f]	Em.:Ex.[g]	Abs.	Abs.	Ex.[h]	Em.[h]
1	$^4I_{9/2}$	$a\Gamma_8$	0	0	0	0	0	0	0
2		Γ_6	97	97[c,e,f]	98				98
3		$b\Gamma_8$		335[c]	342				340
				334[e,f]					
4	$^4I_{11/2}$	$a\Gamma_8$	1921	1920[f]	1924				1921
5		Γ_7	1926	(1931)[f]	1933				1929
6		$b\Gamma_8$	2122	2123[c,f]	2131				2125
				2124[d]					
7		Γ_6	2142	(2136)[d]	2149				2149
				2147[f]					
8	$^4I_{13/2}$	$a\Gamma_7$	(3863)	3861[f]	3867				3862
9		$a\Gamma_8$	(3873)	3870[f]	3875				3869
10		$b\Gamma_7$	4078		4092				4088
11		$b\Gamma_8$	4092	4092[f]	4104				4095
12		Γ_6	4122	4122[f]					4122
13	$^4I_{15/2}$	$a\Gamma_8$	5798	5796[f]	5796				5795
14		Γ_6	(5870)	5869[f]					
15		$b\Gamma_8$	6132	6133[f]	6133				
16		$c\Gamma_8$	6192	6193[f]	6194				
17		Γ_7	6213	6213[f]	6213				
18	$^4F_{3/2}$	Γ_8	11336	11336[f]	11329			11333	11334
				11333[c]					
19	$^4F_{5/2}$	Γ_7	12302	12302[f]	12293	12294	12295	12296	
				12299[e]					
20		Γ_8	12388	12386[f]	12382	12382	12382	12383	
21	$^2H(2)_{9/2}$	Γ_6	(12424)	(12429)[f]	12428		(12412)	12411	
22		$a\Gamma_8$	12537	12536[f]	12527	12527	12528	12528	
23		$b\Gamma_8$	12602	12603[f]	12598	12598	12599	12600	
24	$^4F_{7/2}$	Γ_7	13307	13305[f]	13298	13298	13304	13302	
25		Γ_8	13336	13342[f]	13325	13325	13332	13333	
26		Γ_6		13408[f]	13405	13405	13414	13413	
27	$^4S_{3/2}$	Γ_8	13419	13417[f]		13425		(13422)	
28	$^4F_{9/2}$	Γ_6	14501	14501[f]	14489	14489	14494	14494	
29		$a\Gamma_8$	14563	14562[f]	14552	14552	14557	14557	
30		$b\Gamma_8$	14747	14745[f]	14740	14740	14742	14743	
31	$^2H(2)_{11/2}$	$a\Gamma_8$	15736	15736[f]	15728				
32		Γ_7	15758	(15750)[f]					
33		$b\Gamma_8$	(15913)						
34		Γ_6	15925	15922[f]	(15918)	(15918)	(15919)		
35	$^4G_{5/2}$	Γ_7	16690	16690[f]	16672	16668	16678	16678	
36		Γ_8	16925	16924[f]	16907	16907	16916	16915	
37	$^2G(1)_{7/2}$	Γ_6	(17006)	17005[f]	17017	(17006)			
38		Γ_7	17184	(17188)[f]	17167	17167	17171	17174	
39	$^4G_{5/2}$	Γ_8	17265	17261[f]	17252	17252	17256	17259	
40	$^4G_{7/2}$	Γ_7	18641	18639[d]	18617	18617	18628	18629	18629
41		Γ_8	18793		18768	18771	18779	18778	
42		Γ_6	18870		18850	18850	18861	18859	

TABLE II. (*Continued.*)

			$Cs_2NaNdCl_6$		$Cs_2NaYCl_6:Nd^{3+a}$		$Cs_2NaGdCl_6:Nd^{3+a}$		
No.	$^{2S+1}L_J$	IR	Abs.[b]	Em.[c–f]	Em.:Ex.[g]	Abs.	Abs.	Ex.[h]	Em.[h]
43	$^2K_{13/2}$	$a\Gamma_8$	19167		19147	19146	19154	19155	
44	$^4G_{9/2}$	$a\Gamma_8$	19293		19278	19278		(19273)	
45		Γ_6	19330			(19315)		(19321)	
46		$b\Gamma_8$	19376			19363	19364	19364	
47	$^2K_{13/2}$	$a\Gamma_7$	19380		(19371)	(19375)			
48		$b\Gamma_7$	19676						
49		$b\Gamma_8$	19718			19715	19715	19713	
50		Γ_6	19722						
51	$^2G(1)_{9/2}$	$a\Gamma_8$	20681						
52		$b\Gamma_8$	20826						
53		Γ_6	20962						
54	$^2D(1)_{3/2}$	Γ_8	21014						
55	$^4G_{11/2}$	Γ_6	(21046)						
56		$a\Gamma_8$	21144						
57	$^2K_{15/2}$	Γ_6	21308						
58		$a\Gamma_8$	21367						
59	$^4G_{11/2}$	Γ_7	21367						
60	$^2K_{15/2}$	Γ_7	21523						
61	$^4G_{11/2}$	$b\Gamma_8$	21585						
62	$^2K_{15/2}$	$b\Gamma_8$							
63		$c\Gamma_8$	21732						
64	$^2P_{1/2}$	Γ_6	23043			23032	23031		
65	$^2D(1)_{5/2}$	Γ_7	23595						
66		Γ_8	23625						
67	$^2P_{3/2}$	Γ_8	(25952)			25940			
68	$^4D_{3/2}$	Γ_8	27617	27617[f]		27588	27600		
69	$^4D_{5/2}$	Γ_8	27895			27871	27885		
70		Γ_7	(28062)						
71	$^4D_{1/2}$	Γ_6	28254			28229	28245		
72	$^2I_{11/2}$	Γ_6	28758						
73		$a\Gamma_8$	28805						
74		$b\Gamma_8$	29199						
75		Γ_7	29243			29222			
76	$^2L_{15/2}$	Γ_6	29740						
77		$a\Gamma_8$	29788						
78	$^4D_{7/2}$	Γ_7	29858						
79	$^2L_{15/2}$	Γ_7	29919						
80	$^4D_{7/2}$	Γ_8							
81	$^2L_{15/2}$	$b\Gamma_8$							
82	$^4D_{7/2}$	Γ_6	30143						
83	$^2L_{15/2}$	$c\Gamma_8$							
84	$^2I_{13/2}$	$a\Gamma_7$	30232						
85		Γ_6							
86		$a\Gamma_8$							
87		$b\Gamma_8$	(30481)						
88		$b\Gamma_7$	30574						
89	$^2L_{17/2}$	$a\Gamma_6$	31298						

TABLE II. (*Continued.*)

			$Cs_2NaNdCl_6$		$Cs_2NaYCl_6:Nd^{3+a}$		$Cs_2NaGdCl_6:Nd^{3+a}$		
No.	$^{2S+1}L_J$	IR	Abs.[b]	Em.[c–f]	Em.:Ex.[g]	Abs.	Abs.	Ex.[h]	Em.[h]
90		$a\Gamma_8$	31311						
91		$b\Gamma_8$							
92		$b\Gamma_6$							
93		$c\Gamma_8$							
94		Γ_7							
95	$^2H(1)_{9/2}$	$a\Gamma_8$	32437						
96		$b\Gamma_8$	32538						
97		Γ_6	32538						
98	$^2D(2)_{3/2}$	Γ_8	32905			32874			
99	$^2D(2)_{5/2}$	$a\Gamma_8$	33759						
100	$^2H(1)_{11/2}$	Γ_6							
101	$^2D(2)_{5/2}$	Γ_7	33917						
102	$^2H(1)_{11/2}$	$a\Gamma_8$	(33968)						
103		$b\Gamma_8$	(34024)						
104		Γ_7	(34071)						
105	$^2F(2)_{5/2}$	Γ_8	37838			37803			
106		Γ_7	38109						
107	$^2F(2)_{7/2}$	Γ_6	(39232)						
108		Γ_8	39267						
109		Γ_7	(39449)						

[a]IR irreducible representation; Abs. 10 K absorption spectrum (except for $^4I_{11/2}$ at 85 K); Em. 10 K emission; Ex. 10–15 K excitation spectra.
[b]The underlined values from the absorption spectra are mean values of zero phonon lines split by 2–3 cm^{-1}.
[c]Mean values of (inferred) zero phonon lines in the emission from $^4F_{3/2}\Gamma_8$
[d]Mean values of (inferred) zero phonon lines in the emission from $^4G_{5/2}\Gamma_7$.
[e]Mean values of (inferred) zero phonon lines in the emission from $^4F_{5/2}\Gamma_7$.
[f]Mean values of (inferred) zero phonon lines in the emission from $^4D_{3/2}\Gamma_8$.
[g]The emission results are from this study using $Cs_2NaY_{0.97}Nd_{0.03}Cl_6$. A comparison has been made with Ref. 17 by subtracting 36 cm^{-1} from each of the levels 18–26 therein, and ~10 cm^{-1} from levels 28–44 therein. This shows good agreement except for the calibration differences. The assigned symmetry representations have been changed from those in Ref. 17 for the underlined values.
[h]From Ref. 19. Values in parentheses are tentative assignments.

$^2H(2)_{9/2}$ (which is mixed with the ground state by spin-orbit coupling and *J*-mixing) overlaps the associated vibronic structure of these two former transitions. The assignment of the transitions to the $^2H(2)_{9/2}a\Gamma_8, b\Gamma_8$ crystal field levels is clear but that to Γ_6 is tentative.

The region between 13 309 and 13 697 cm^{-1}, Fig. 2(f), comprises the transitions to $^4F_{7/2}$ and $^4S_{3/2}$. The ZPL and vibronic structures of two transitions to $^4F_{7/2}$ are well resolved and the highest energy transition is assigned to $^4S_{3/2}$, rather than to $^4F_{7/2}$, because of evidence from the $^4D_{3/2}$ emission spectrum, discussed subsequently. The assignments for the transition to $^4F_{9/2}$, Fig. 2(g), are straightforward and this spectrum has been shown in more detail previously.[20] The next group of bands is very weak, Fig. 2(h), and corresponds to the $^4I_{9/2} \rightarrow {}^2H(2)_{11/2}$ transition between 15 735 and 16 190 cm^{-1}. The multiplet $^2H(2)_{11/2}$ is split into four crystal field states with the upper two close together (Γ_6 and $b\Gamma_8$), as are the lower two states (Γ_7 and $a\Gamma_8$), but a different order has been previously calculated.[17,19] The lower level is now assigned to $a\Gamma_8$ following the present calculation in Sec. V. Then, three transitions are readily assigned from the vibronic structure, with each of the ZPL split by 2–3 cm^{-1}. The highest energy transition has the ZPL at 15 925 cm^{-1} and is assigned to $^2H(2)_{11/2}\Gamma_6$. The location of the fourth transition [to $^2H(2)_{11/2}b\Gamma_8$] is ambiguous. One tentative assignment of $b\Gamma_8$ is to the band at 15 913 cm^{-1} in Fig. 2(h).

C. Transitions to $^4G_J(J=5/2,7/2,9/2,11/2)$, $^2G(1)_J(J=7/2,9/2)$, $^2D(1)_{3/2}$, and $^2K_J(J=13/2,15/2)$

The transitions to ^4G_J multiplets are hypersensitive transitions ($|\Delta L| \leqslant 2$, $\Delta S=0$, $|\Delta J| \leqslant 2$),[35] which are found to have strong, clearly-resolved vibronic features. The bands between 16 691 and 17 544 cm^{-1}, Fig. 2(i), are clearly assigned as transitions to the $^4G_{5/2}$ and $^2G(1)_{7/2}$ multiplets, except for those tentatively assigned to the $^2G(1)_{7/2}\Gamma_6$ transition. The three crystal field levels of $^4G_{7/2}$ are clearly identified from the vibronic structure between 18 641 and 19 149 cm^{-1} in

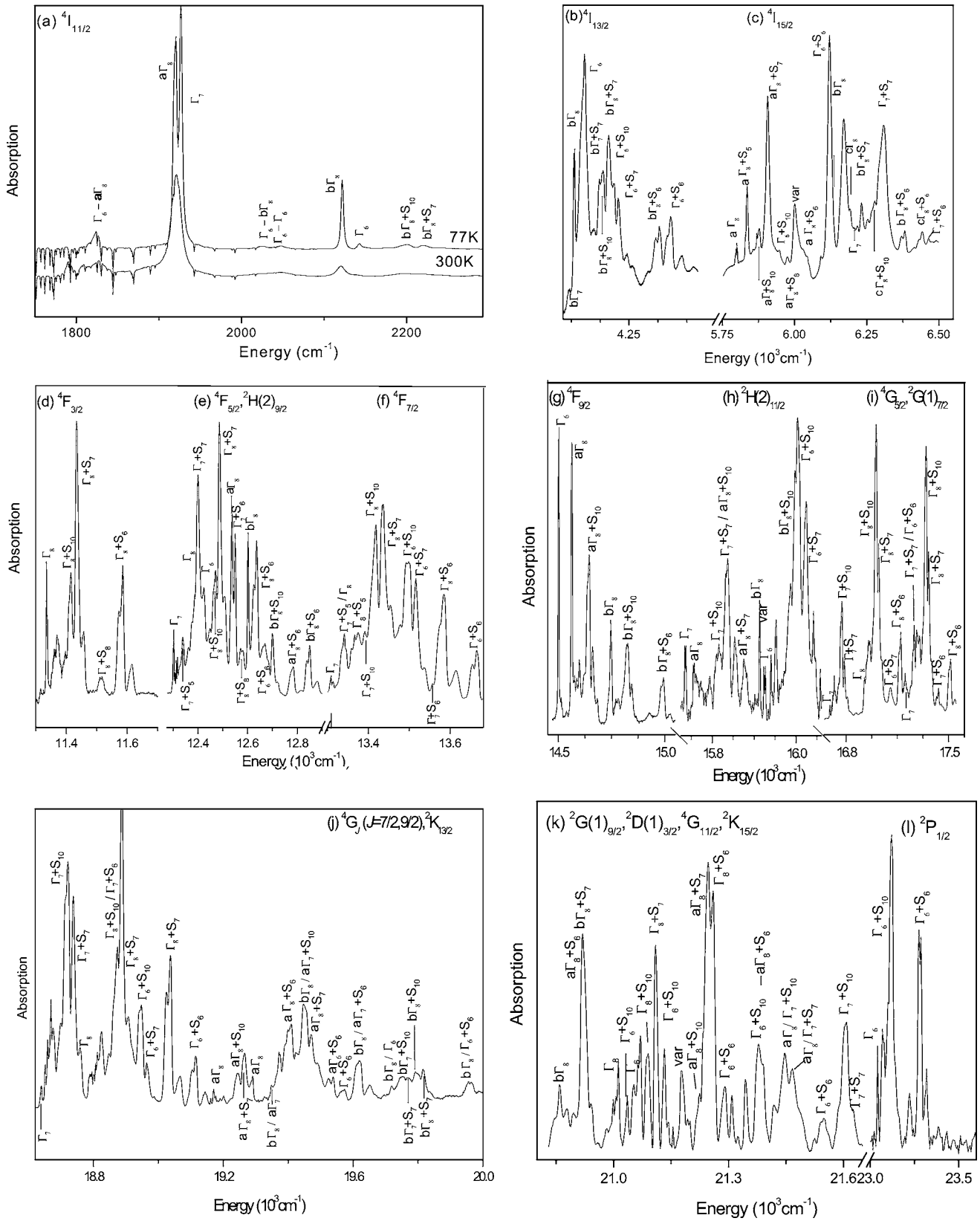

FIG. 2. Absorption spectra of $Cs_2NaNdCl_6$. [The temperature is 10 K except for (a). Only terminal states are identified in most cases since the initial state is $^4I_{9/2}a\Gamma_8$, or as marked. var variable intensity.]

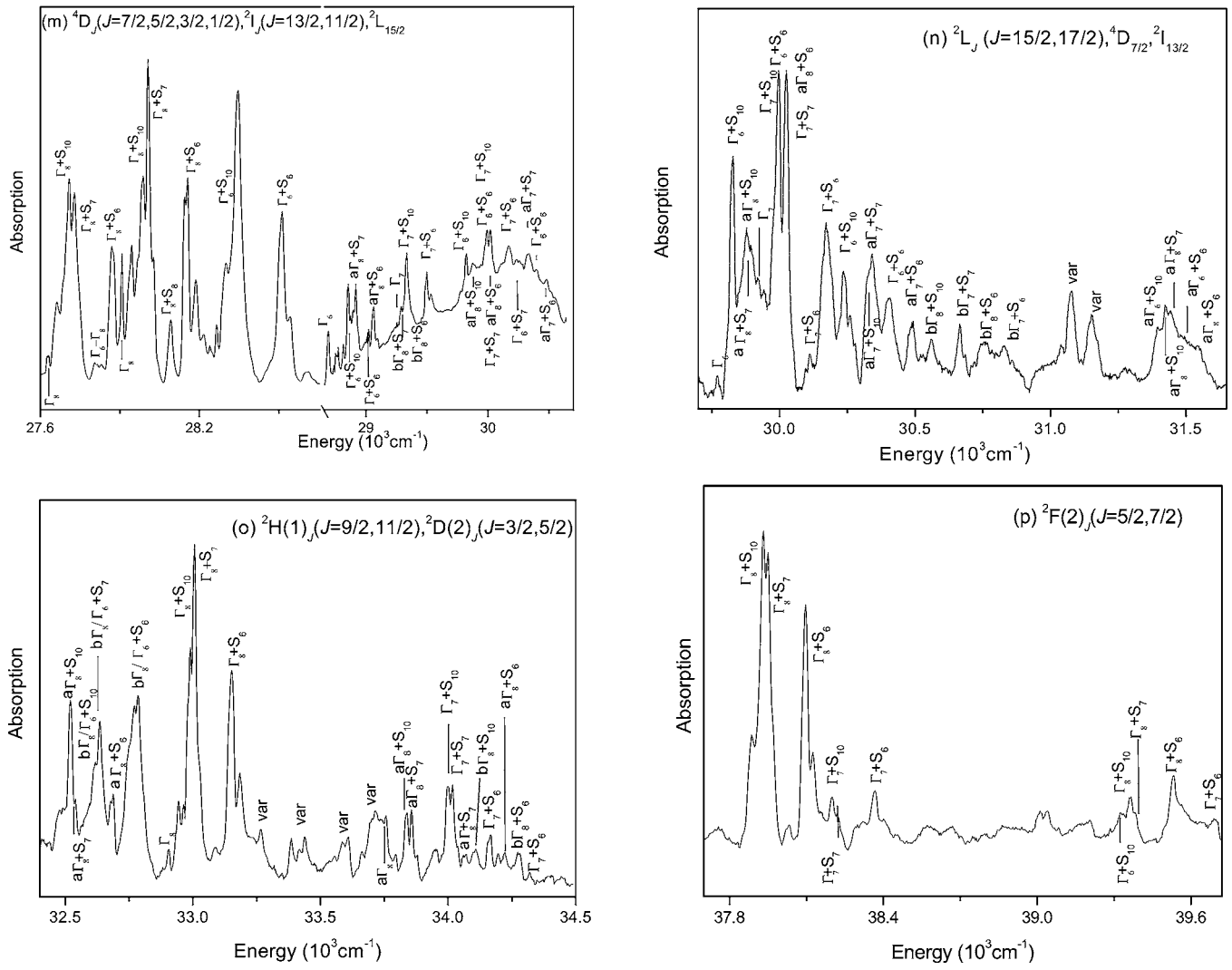

FIG. 2. (*Continued*).

Fig. 2(j). The excited multiplet term $^4G_{9/2}$ also consists of three crystal field levels in the order $a\Gamma_8 < \Gamma_6 < b\Gamma_8$. The magnetic dipole allowed origins are observed with weak intensities between 19 293 and 19 376 cm^{-1} and the three transitions are also clearly identified from the vibronic structure, Fig. 2(j). In this region, transitions are also observed to the $^2K_{13/2}$ levels, also in Fig. 2(j).

The transitions in the region above 20 681 cm^{-1}, Fig. 2(k), are rather more congested and the terminal crystal field states are of mixed *SLJ* parentage. The first two transitions are readily identified from the ZPL (at 20 681 and 20 826 cm^{-1}), and associated vibronic structure, and are assigned to the terminal $^2G(1)_{9/2}a\Gamma_8, b\Gamma_8$ states. The remaining energy level assignments (Table II) can consistently account for all of the observed bands in this region but are not unambiguous. The strongest features are assigned to the terminal vibronic states $^2D(1)_{3/2}\Gamma_8+S_7, S_6$ (at 21 112, ~21 262 cm^{-1}), $^2K_{15/2}\Gamma_6+S_{10}$ (at 21 382 cm^{-1}), $^2K_{15/2}\Gamma_7+S_{10}$ (at 21 607 cm^{-1}). The $^2K_{15/2}a\Gamma_8$ and $^4G_{11/2}\Gamma_7$ states are assumed to be coincident and give S_{10} and S_6 vibronic origins at 21 451, 21 473 cm^{-1}, respectively in Fig. 2(k).

D. Transitions to $^2P_J(J=1/2,3/2)$ and $^2D(1)_{5/2}$

Figure 2(l) shows part of the region between 23 040 and 24 000 cm^{-1} and is dominated by the vibronic structure of the $^4I_{9/2}a\Gamma_8 \rightarrow {}^2P_{1/2}\Gamma_6$ transition, for which the ZPL is located at 23 043 cm^{-1}. Additional features are observed in thicker crystals at ~275 cm^{-1} to high energy of the strong bands which either correspond to the S_1 progression on these features or to an impurity. Some weak features are observed between 23 600 and 23 900 cm^{-1} in the thick crystals. These are assigned to the vibronic structure of two transitions to $^2D(1)_{5/2}$ with inferred origins at 23 595 and 23 625 cm^{-1}. Further weak bands are observed near 26 000 cm^{-1}, with the possible assignments to S_7, S_{10}, and S_6 vibronic origins of an origin inferred to be at 25 952 cm^{-1} ($^2P_{3/2}\Gamma_8$), but some additional unassigned lines are present.

E. Transitions to $^4D_J(J=3/2,5/2,1/2)$

The first part of Fig. 2(m) shows the transitions to $^4D_J(J=3/2,5/2,1/2)$ between 27 600–28 600 cm^{-1}. The first group of bands corresponds to the $^4I_{9/2}a\Gamma_8 \rightarrow {}^4D_{3/2}\Gamma_8$ transition. The MD allowed ZPL is observed to be split by

6 cm^{-1} near 27 620 cm^{-1}, and the S_{10}, S_7, and S_6 vibronic sidebands appear to high energy. The sharp line in Fig. 2(m) at 27 985 cm^{-1} is assigned as the origin of the transition terminating upon $^4D_{5/2}\Gamma_8$ and the associated vibronic structures are also indicated. Another sharp line at 28 062 cm^{-1} with variable intensity [not evident in Fig. 2(m)], is tentatively assigned to the origin of the transition to $^4D_{5/2}\Gamma_7$, or a related defect site. The $^4D_{1/2}\Gamma_6$ level is located at 28 254 cm^{-1} but the vibronic sideband is not well resolved.

F. Transitions to $^2I_J(J=11/2,13/2)$, $^2L_J(J=15/2,17/2)$, and $^4D_{7/2}$

The next excited term is $^2I_{11/2}$, which is about 500 cm^{-1} higher in energy than $^4D_{1/2}$. There are several variable intensity bands between 28 600 and 28 750 cm^{-1}. The first two crystal field levels, Γ_6 and $a\Gamma_8$, are calculated to be at rather lower energy than the closely-separated $b\Gamma_8$, Γ_7 crystal field levels, so that the transitions are readily assigned to features between 28 758 and 29 080 cm^{-1} [Fig. 2(m)]. One further transition to an upper level of $^2I_{11/2}$ is readily identified from the ZPL (at 29 243 cm^{-1}), S_{10} and S_6 structure. The terminal level is assigned to Γ_7 because a weak origin at 44 cm^{-1} to lower energy can be associated with S_{10} and S_6 structure.

The region between 29 740 and 30 670 cm^{-1} [Figs. 2(m) and 2(n)] comprises no fewer than 14 transitions to the crystal field levels of $^2L_{15/2}$, $^4D_{7/2}$, and $^2I_{13/2}$ multiplets. It is therefore not surprising that the overlapping transitions give rise to rather broad, unresolved features. The lowest energy transition has the ZPL ($a\Gamma_8 \rightarrow {}^2L_{15/2}\Gamma_6$) at 29 740 cm^{-1}, with associated S_7 and S_6 structure to high energy. The transitions to the next three levels ($a\Gamma_8, 2\Gamma_7$) are assigned from the vibronic structure, Fig. 2(n). The highest energy transition (to $^2I_{13/2}b\Gamma_7$) is clearly identified from the S_{10}, S_7 structure, with the (unobserved) electronic origin inferred to be at 30 574 cm^{-1}. Two further transitions are located from vibronic structure and assigned to $^4D_{7/2}\Gamma_6$ and $^2I_{13/2}a\Gamma_7$ on the basis of the calculation.

There are some variable intensity features which are not assigned to $Cs_2NaNdCl_6$ at 31 066, 31 141 cm^{-1}. To higher energy, Fig. 2(n), two further, weak transitions are assigned to the $^2L_{17/2}a\Gamma_6, a\Gamma_8$ terminal states.

G. Transitions to $^2H(1)_J(J=9/2,11/2)$, $^2D(2)_J(J=3/2,5/2)$

The next group of bands, Fig. 2(o), is between 32 400 and 33 420 cm^{-1}, and corresponds to the transitions to terminal $^2H(1)_{9/2}$ and $^2D(2)_{3/2}$ terms. From the vibronic structures, three transitions are clearly identified. Since the $^2H(1)_{9/2}b\Gamma_8, \Gamma_6$ states are calculated to be virtually coincident, the middle transition is associated with both of these terminal states.

Two transitions to $^2D(2)_{5/2}$ in Fig. 2(o) exhibit fairly complete vibronic sidebands and the origins are assigned to $a\Gamma_8$(33 759 cm^{-1}) and Γ_7(33 917 cm^{-1}). The three highest energy bands have been tentatively assigned to the S_6 vibronic origins of three further electronic transitions of $^2H(1)_{11/2}$ (to $a\Gamma_8$, $b\Gamma_8$, Γ_7).

H. Transitions to $^2F(2)_J(J=5/2,7/2)$

The vibronic sideband of $^4I_{9/2} \rightarrow {}^2F(2)_{5/2}\Gamma_8$ is about 6 times stronger than that of $^4I_{9/2} \rightarrow {}^2F(2)_{5/2}\Gamma_7$ [Fig. 2(p)]. The transition to $^2F(2)_{7/2}\Gamma_8$ is clearly observed and a further two transitions are tentatively assigned. The $4f^3$-$4f^2 5d$ transition of $Cs_2NaNdCl_6$ occurs above 46 000 cm^{-1}.[23] Thus the onset of intense absorption above 39 750 cm^{-1} is attributed to the $4f^2$-$4f5d$ transition of traces of Pr^{3+} impurity in the crystals.[36]

IV. EMISSION SPECTRA OF $Cs_2NaNdCl_6$

In the absence of restrictive selection rules (such as for $J=0$ to $J=1$ transitions) and concentration quenching effects, luminescence occurs from suitably populated states which are separated from the next-lowest states by 5 quanta (or more) of the highest energy vibrational mode.[18] For $Cs_2NaNdCl_6$ this amounts to an energy gap greater than $\approx$1130 cm^{-1}, so that from the calculated energy level scheme (Fig. 1 and Table III), luminescence is expected from $^4F_{3/2}$, $^4G_{7/2}$, $^2P_{1/2}$, $^2P_{3/2}$, $^4D_{3/2}$, and $^2F(2)_{5/2}$ purely on the basis of the energy level gaps. However, one-phonon-assisted cross-relaxation processes can readily be postulated for $^2P_{1/2}$, $^2P_{3/2}$, so that the failure to observe luminescence from these multiplets under 355 nm excitation of neat $Cs_2NaNdCl_6$ was not surprising. This excitation energy is not high enough to populate $^2F(2)_{5/2}$, but a resonant cross-relaxation process [to $^4I_{13/2}$ and $^2D(2)_{5/2}$] and several non-resonant processes are also operative for this multiplet term in neat $Cs_2NaNdCl_6$. Thus, as expected, luminescence was detected and analyzed in $Cs_2NaNdCl_6$ from $^4F_{3/2}$, $^4G_{7/2}$, and $^4D_{3/2}$ in this study. Although the nonradiative decay from $^4F_{5/2}$ to $^4F_{3/2}$ requires only four phonons, weak luminescence is also reported from $^4F_{5/2}$ at low temperatures. Previous studies have described the luminescence from $^4F_{3/2}$ in $Cs_2NaNdCl_6$ (Ref. 21) and $Cs_2NaLaCl_6:Nd^{3+}$;[22] $^4D_{3/2}$ (in part) and $^4G_{7/2}$ in $Cs_2NaYCl_6:Nd^{3+}$;[17] and $^4G_{7/2}$, $^4F_{3/2}$ in $Cs_2NaGdCl_6:Nd^{3+}$.[18,19] In the following, the fluorescence from neat $Cs_2NaNdCl_6$ is described and assigned to the $^4F_{3/2}$, $^4F_{5/2}$, $^4G_{7/2}$, and $^4D_{3/2}$ multiplet terms. Under 355 nm excitation of $Cs_2NaYCl_6:Nd^{3+}$ at 10 K we additionally observe luminescence transitions from $^2P_{3/2}\Gamma_8$ located at 25 940 cm^{-1}. Some of these transitions are weak or are obscured by other transitions, but the $^2P_{3/2}\Gamma_8$ transitions terminating upon $^4I_{13/2}$, $^4F_{3/2}$, $^4F_{5/2}$, and $^2H(2)_{9/2}$ have all been assigned. We mainly focus upon the detailed emission spectra from $^4D_{3/2}$ which have not been previously reported.

A. Emission from $^4F_{3/2}$, $^4F_{5/2}$

The first group of emission bands from $^4F_{3/2}$ under 514.5 nm excitation at 10 K is shown in Fig. 3(a). The ZPL of the transitions to the $^4I_{9/2}a\Gamma_8, b\Gamma_8$ states are each split and some of the vibronic transitions are marked in the figure. To lower energy the transitions to $^4I_{11/2}a\Gamma_8, \Gamma_7$ are unresolved with S_{10}, S_7, and S_6 vibronic structure, and the transitions to $^4I_{11/2}$ $b\Gamma_8 + S_{10}, S_7, S_6$ are also observed. Under 355 nm excitation at the nominal temperature 10 K, weak emission with extensive vibronic structure was also observed in the transi-

TABLE III. Experimental and calculated energy levels (in cm^{-1}) and differences Δ (in cm^{-1}) of Nd^{3+} in $Cs_2NaNdCl_6$.

No.	$^{2S+1}L_J$	IR	Expt.	Calc. $E1$ $4f^2$	(Δ)	Calc. $E2$ $4f^2np$	(Δ)
1	$^4I_{9/2}$	$a\Gamma_8$	0	9	−9	5	−5
2		Γ_6	97	92	5	100	−3
3		$b\Gamma_8$	335	344	−9	339	−4
4	$^4I_{11/2}$	$a\Gamma_8$	1921	1911	11	1915	6
5		Γ_7	1926	1919	7	1923	3
6		$b\Gamma_8$	2122	2125	−3	2119	3
7		Γ_6	2142	2153	−11	2143	−1
8	$^4I_{13/2}$	$a\Gamma_7$	3861	3849	12	3856	5
9		$a\Gamma_8$	3870	3856	14	3864	6
10		$b\Gamma_7$	4078	4088	−10	4083	−5
11		$b\Gamma_8$	4092	4096	−4	4088	4
12		Γ_6	4122	4131	−9	4120	2
13	$^4I_{15/2}$	$a\Gamma_8$	5797	5793	4	5799	−2
14		Γ_6	5869	5862	7	5875	−6
15		$b\Gamma_8$	6132	6137	−5	6131	1
16		$c\Gamma_8$	6192	6202	−10	6194	−2
17		Γ_7	6213	6210	3	6210	3
18	$^4F_{3/2}$	Γ_8	11335	11324	11	11336	−1
19	$^4F_{5/2}$	Γ_7	12302	12277	25	12308	−6
20		Γ_8	12387	12380	7	12386	1
21	$^2H(2)_{9/2}$	Γ_6	(12426)	12487	−61	12421	5
22		$a\Gamma_8$	12537	12497	40	12536	1
23		$b\Gamma_8$	12602	12610	−7	12604	−2
24	$^4F_{7/2}$	Γ_7	13306	13314	−8	13310	−4
25		Γ_8	13339	13341	−2	13348	−9
26		Γ_6	13408	13398	10	13401	7
27	$^4S_{3/2}$	Γ_8	13418	13400	19	13414	4
28	$^4F_{9/2}$	Γ_6	14501	14509	−8	14504	−3
29		$a\Gamma_8$	14563	14564	−1	14562	1
30		$b\Gamma_8$	14746	14741	5	14745	1
31	$^2H(2)_{11/2}$	$a\Gamma_8$	15736	15815	−79	15752	−16
32		Γ_7	15758	15837	−79	15764	−6
33		$b\Gamma_8$	(15913)	15846	67	15931	−18
34		Γ_6	15925	15872	53	15946	−21
35	$^4G_{5/2}$	Γ_7	16690	16719	−29	16719	−29
36		Γ_8	16925	16940	−15	16940	−15
37	$^2G(1)_{7/2}$	Γ_6	(17006)	17077	−71	17029	−23
38		Γ_7	17184	17097	87	17165	19
39	$^4G_{5/2}$	Γ_8	17263	17256	7	17255	8
40	$^4G_{7/2}$	Γ_7	18640	18639	1	18629	11
41		Γ_8	18793	18820	−17	18800	−7
42		Γ_6	18870	18904	−34	18882	−12
43	$^2K_{13/2}$	$a\Gamma_8$	19167	19156	11	19165	2
44	$^4G_{9/2}$	$a\Gamma_8$	19293	19306	−13	19287	6
45		Γ_6	19330	19340	−10	19323	7
46		$b\Gamma_8$	19376	19350	27	19375	1

TABLE III. (*Continued.*)

No.	$^{2S+1}L_J$	IR	Expt.	Calc. $E1$ $4f^2$	(Δ)	Calc. $E2$ $4f^2np$	(Δ)
47	$^2K_{13/2}$	$a\Gamma_7$	19380	19370	10	19378	2
48		$b\Gamma_7$	19676	19599	78	19638	38
49		$b\Gamma_8$	19718	19700	18	19716	2
50		Γ_6	19722	19741	−19	19726	−4
51	$^2G(1)_{9/2}$	$a\Gamma_8$	20681	20646	35	20664	17
52		$b\Gamma_8$	20826	20847	−21	20835	−9
53		Γ_6	20962	20967	−5	20943	19
54	$^2D(1)_{3/2}$	Γ_8	21014	21028	−14	21009	5
55	$^4G_{11/2}$	Γ_6	(21046)	21047	−1	21040	6
56		$a\Gamma_8$	21144	21149	−5	21155	−11
57	$^2K_{15/2}$	Γ_6	21308	21266	42	21291	17
58		$a\Gamma_8$	21367	21330	37	21362	5
59	$^4G_{11/2}$	Γ_7	21367	21374	−7	21371	−4
60	$^2K_{15/2}$	Γ_7	21523	21498	25	21507	16
61	$^4G_{11/2}$	$b\Gamma_8$	21585	21596	−11	21585	0
62	$^2K_{15/2}$	$b\Gamma_8$		21659		21689	
63		$c\Gamma_8$	21732	21743	−11	21738	−6
64	$^2P_{1/2}$	Γ_6	23043	23031	12	23034	9
65	$^2D(1)_{5/2}$	Γ_7	23595	23596	0	23602	−7
66		Γ_8	23625	23666	−41	23633	−8
67	$^2P_{3/2}$	Γ_8	(25952)	25991	−39	25967	−15
68	$^4D_{3/2}$	Γ_8	27617	27601	16	27604	13
69	$^4D_{5/2}$	Γ_8	27895	27846	49	27869	26
70		Γ_7	(28062)	28090	−28	28077	−15
71	$^4D_{1/2}$	Γ_6	28254	28257	−3	28271	−17
72	$^2I_{11/2}$	Γ_6	28758	28753	5	28740	18
73		$a\Gamma_8$	28805	28806	−1	28781	24
74		$b\Gamma_8$	29199	29203	−3	29212	−13
75		Γ_7	29243	29217	26	29221	22
76	$^2L_{15/2}$	Γ_6	29740	29785	−45	29758	−18
77		$a\Gamma_8$	29788	29817	−29	29801	−13
78	$^4D_{7/2}$	Γ_7	29858	29849	10	29869	−11
79	$^2L_{15/2}$	Γ_7	29919	29900	19	29913	6
80	$^4D_{7/2}$	Γ_8		30009		30027	
81	$^2L_{15/2}$	$b\Gamma_8$		30035		30046	
82	$^4D_{7/2}$	Γ_6	30143	30145	−2	30125	−18
83	$^2L_{15/2}$	$c\Gamma_8$		30162		30171	
84	$^2I_{13/2}$	$a\Gamma_7$	30232	30228	4	30230	2
85		Γ_6		30231		30237	
86		$a\Gamma_8$		30265		30270	
87		$b\Gamma_8$	(30481)	30521	−40	30514	−33
88		$b\Gamma_7$	30574	30613	−39	30608	−34
89	$^2L_{17/2}$	$a\Gamma_6$	31298	31309	−11	31298	0
90		$a\Gamma_8$	31311	31327	−6	31319	−8
91		$b\Gamma_8$		31394		31412	
92		$b\Gamma_6$		31453		31480	
93		$c\Gamma_8$		31573		31572	
94		Γ_7		31583		31578	

TABLE III. (*Continued.*)

No.	$^{2S+1}L_J$	IR	Expt.	Calc. $E1$ $4f^2$	(Δ)	Calc. $E2$ $4f^2np$	(Δ)
95	$^2H(1)_{9/2}$	$a\Gamma_8$	32437	32483	−46	32459	−22
96		$b\Gamma_8$	32538	32515	23	32533	5
97		Γ_6	32538	32540	−2	32543	−5
98	$^2D(2)_{3/2}$	Γ_8	32905	32915	−10	32892	13
99	$^2D(2)_{5/2}$	$a\Gamma_8$	33759	33744	15	33750	9
100	$^2H(1)_{11/2}$	Γ_6		33877		33891	
101	$^2D(2)_{5/2}$	Γ_7	33917	33893	24	33911	6
102	$^2H(1)_{11/2}$	$a\Gamma_8$	(33968)	33913	56	33954	14
103		$b\Gamma_8$	(34024)	33975	50	34011	13
104		Γ_7	(34071)	34075	−4	34053	18
105	$^2F(2)_{5/2}$	Γ_8	37838	37920	−82	37845	−7
106		Γ_7	38109	38020	89	38126	−17
107	$^2F(2)_{7/2}$	Γ_6	(39232)	39281	−49	39207	25
108		Γ_8	39267	39297	−29	39260	7
109		Γ_7	(39449)	39418	31	39459	−10

tions from $^4F_{5/2}\Gamma_7$ to the crystal field states of $^4I_{9/2}$ (not shown). In this case, the vibronic transitions to the $b\Gamma_8$ terminal state are weaker than those to $a\Gamma_8$ and Γ_6. Emission from Yb^{3+} trace impurity is observed below 10 252 cm^{-1} and this has previously been described.[37]

B. Emission from $^4G_{7/2}\Gamma_7$

Weak emission from $^4G_{7/2}$ is observed under 355 and 514.5 nm excitation. Under the latter excitation wavelength, Fig. 3(b) shows the transition terminating upon $^4I_{11/2}$ and nearly all of the vibronic intensity arises from the $b\Gamma_8$ terminal state.

C. Emission from $^4D_{3/2}$

Under 355 nm excitation at 10 K, emission is observed from $^4D_{3/2}$ to the lower multiplet terms. The transitions to ^4I_J ($J=9/2,11/2,13/2,15/2$) are shown in Figs. 3(c)–3(f). All bands have been assigned. The stronger (or more important) features are marked and the derived crystal field energy levels of ^4I_J are listed in Table II. Many of the ZPL are split by 7 cm^{-1} and this is attributed to the Γ_8 excited state splitting into two Kramers doublets. Figure 3(c) shows the first group of bands in the emission from $^4D_{3/2}\Gamma_8$. The transitions to $^4I_{9/2}a\Gamma_8, b\Gamma_8$ are readily observed, but that to Γ_6 is almost silent. In this figure, Fig. 3(c), the relative intensities of the first members of the weak progression in S_1 which are observed infer a coordinate displacement of 2.4±0.2 pm (i.e., a bond length change of ~1 pm)[38] between the two high spin states $^4D_{3/2}\Gamma_8$ and $^4I_{9/2}b\Gamma_8$. The derived progression frequency is 280 cm^{-1} in the $^4I_{9/2}b\Gamma_8$ state, which is 5 cm^{-1} less than that deduced for the $^4I_{9/2}a\Gamma_8$ state from the progressions. The latter frequency, 285 cm^{-1}, is the same as the Raman S_1 frequency (of the $a\Gamma_8$ state) at this temperature[24] so that anharmonicity effects are small. The transition from $^4D_{3/2}$ to $^4I_{11/2}$ is shown in Fig. 3(d) and the strongest vibronic structure is associated with the terminal $a\Gamma_8$ and $b\Gamma_8$ states. Again, very weak progressions in S_1 are observed to low energy of the group of bands, with the progression frequencies 280 and 285 cm^{-1}, respectively, for the $a\Gamma_8$ and $b\Gamma_8$ states of $^4I_{11/2}$. Figures 3(e) and 3(f) show the transitions terminating upon $^4I_{13/2}$ and $^4I_{15/2}$, with the latter being weaker. Figure 3(g) shows the transition terminating upon $^4F_{3/2}$. It is interesting to compare the emission in Fig. 3(g) (under 355 nm excitation) with that in Fig. 3(b) (under 514.5 nm excitation). In Fig. 3(g), the emission from $^4G_{5/2}$ is weak and overshadowed by the $^4D_{3/2}\Gamma_8 \rightarrow {}^4F_{3/2}\Gamma_8$ transition, which has maximum intensity near 16 200 cm^{-1}. In this case there are no overlapping transitions and the splitting of the lower and upper Γ_8 states into Kramers doublets is resolved. Just to lower energy, Fig. 3(h), the more complex transitions to $^4F_{5/2}$ and $^2H(2)_{9/2}$ are observed. From the ZPL and vibronic structures, four electronic transitions are clearly assigned. A further transition (to $^4F_{5/2}\Gamma_6$) is more tentative but otherwise the medium intensity band at 14 939 cm^{-1} cannot be assigned.

The next group of bands, Fig. 3(i), corresponds to the $^4D_{3/2}\Gamma_8 \rightarrow {}^4F_{7/2}, {}^4S_{3/2}$ transitions. The lower energy bands are readily associated with the origins and vibronic structures of the transitions terminating upon $^4F_{7/2}\Gamma_7, \Gamma_8$. However, the splittings of the vibronic structure for further transitions indicate that two further states are involved, for which the electronic origins are assigned to $^4D_{3/2}\Gamma_8 \rightarrow {}^4F_{7/2}\Gamma_6$ at 14 206 cm^{-1}, and $^4D_{3/2}\Gamma_8 \rightarrow {}^4S_{3/2}\Gamma_8$ at 14 197 cm^{-1}. In Fig. 3(j), the highest energy ZPL, $^4D_{3/2}\Gamma_8 \rightarrow {}^4F_{9/2}\Gamma_6$, clearly shows the excited state splitting into Kramers doublets. The bands in this figure are readily assigned to three electronic transitions, as marked.

To lower energy, two further groups of weak bands are assigned to $^4D_{3/2}$ emission (not shown). The first of these

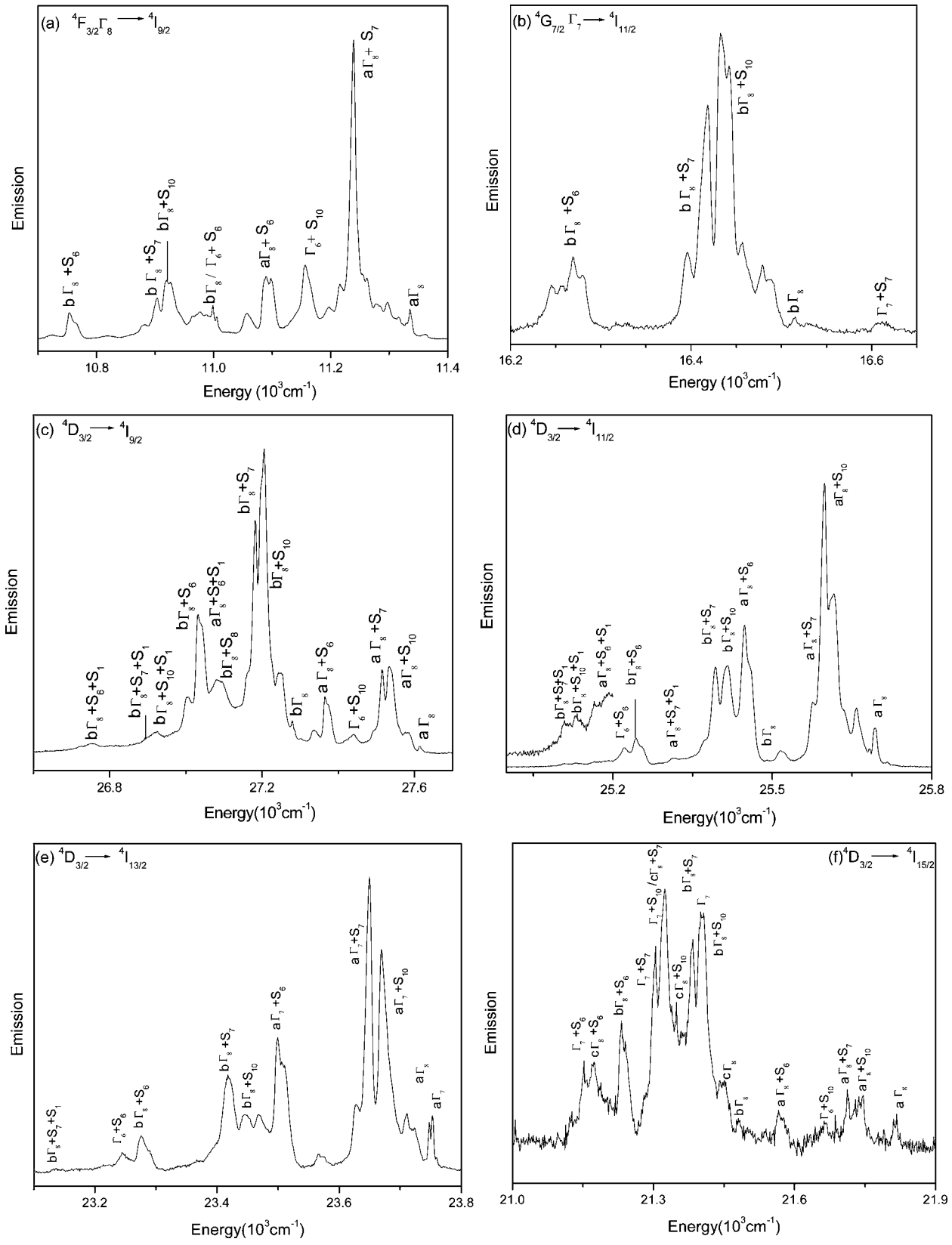

FIG. 3. 10 K emission spectra of $Cs_2NaNdCl_6$ (a), (b) under 514.5 nm excitation; (c)–(j) under 355 nm excitation. The terminal states are marked. The initial state in (c)–(j) is $^4D_{3/2}\Gamma_8$ except for the overlap as shown in (g).

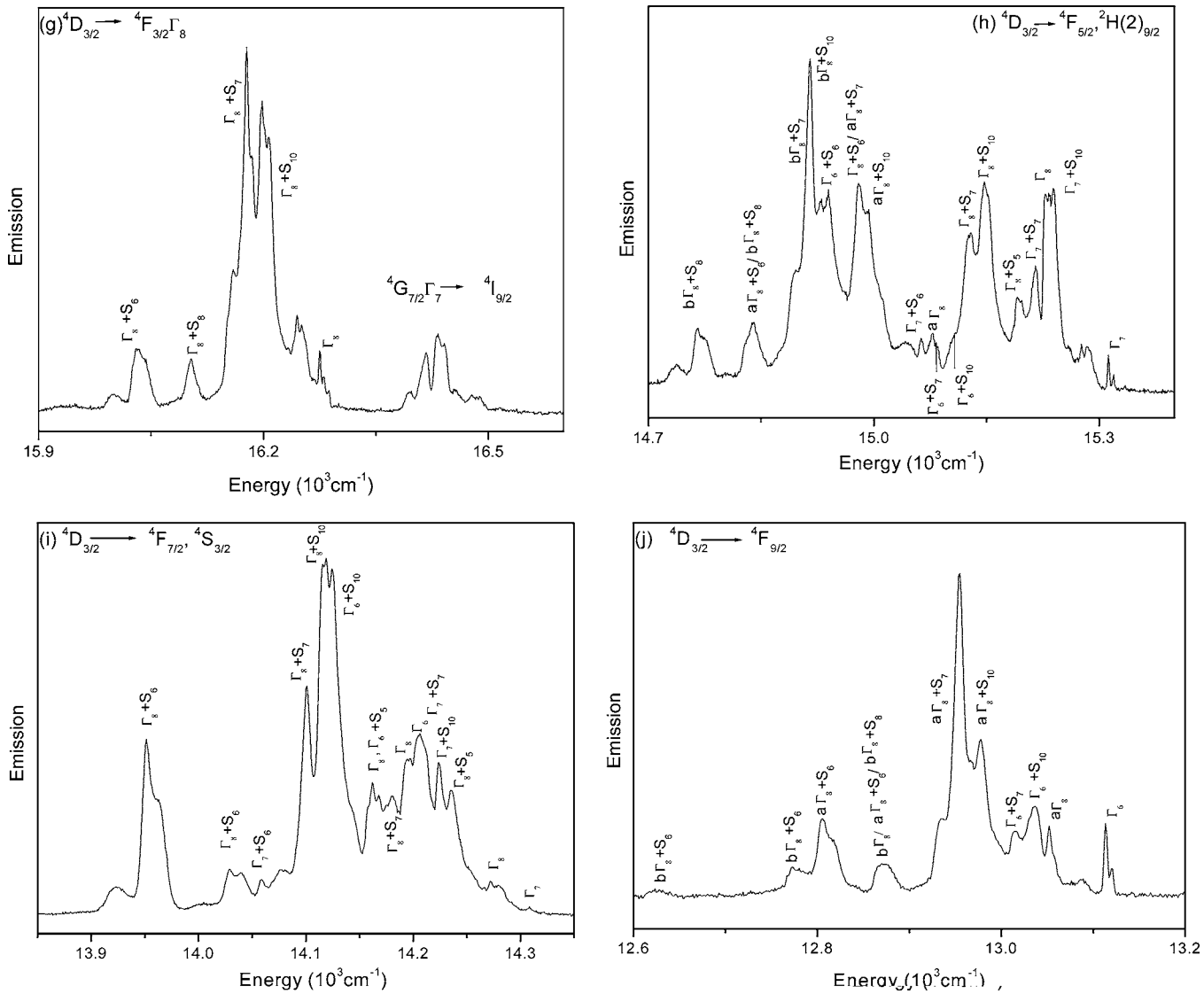

FIG. 3. (*Continued*).

groups, between 11 883 and 11 443 cm^{-1}, partly overlaps the $^4F_{5/2} \rightarrow {}^4I_{9/2}$ transition, but the vibronic structures of $^4D_{3/2}\Gamma_8 \rightarrow {}^2H(2)_{11/2}a\Gamma_8, \Gamma_6$ are observed. The second weak group of bands overlaps the low energy part of the $^4F_{3/2} \rightarrow {}^4I_{9/2}$ transition and comprises the transitions to $^4G_{5/2}$ and $^2G(1)_{7/2}$.

D. Comparison with the absorption and excitation spectrum of $Cs_2NaYCl_6:Nd^{3+}$ and the absorption, excitation, and emission spectra of $Cs_2NaGdCl_6:Nd^{3+}$

Doping Nd^{3+} into the host lattices $Cs_2NaLnCl_6$ (Ln=Gd, Y) has the advantage that it is situated at a perfectly octahedral site of symmetry so that the spectra do not show the band splittings present for $Cs_2NaNdCl_6$. There are some other bonuses since the vibronic fingerprints are rather different and provide clear confirmation of the locations of electronic origins.

There is one point which illustrates the above sentence and is worth mentioning in more detail. The shape and position of the S_{10} mode, which is often the strongest feature in a vibronic sideband, vary considerably for the three systems studied. This feature appears at 75, 81 cm^{-1} below the electronic origin in $Cs_2NaNdCl_6$, and at 68, 77 cm^{-1} in $Cs_2NaGdCl_6:Nd^{3+}$ (Table I). In both cases the higher energy feature is strongest. However the guest-host coupling and the dispersion are both of less importance in $Cs_2NaYCl_6:Nd^{3+}$, where the low-energy feature at 69 cm^{-1} is much stronger than the broad shoulder at 80 cm^{-1}. The strong band is identified as the $k=0$ S_{10} mode. It is possible therefore that the weaker, lower energy feature at 75 cm^{-1} in $Cs_2NaNdCl_6$ corresponds to S_{10}, and the upper stronger band to a zone boundary mode, just as in the model calculation of the Cs_2UBr_6 vibronic sideband.[24,39]

We have investigated the 355 nm excited luminescence of $Cs_2NaYCl_6:Nd^{3+}$ in the region between 27 500 to 8 700 cm^{-1}. The assignments confirm those for neat $Cs_2NaNdCl_6$ and in addition the emission from $^2P_{3/2}$ (populated by nonradiative decay from $^4D_{3/2}$) to lower levels was observed. The 10 K excitation and 4.2 K emission spectra of

$Cs_2NaYCl_6:Nd^{3+}$ were reported by Foster *et al.*[17] and 32 energy levels of Nd^{3+} in this system were deduced. These values are similar, with four exceptions, to those in Table II when a recalibration of 36 cm^{-1} is made for levels 18–26 in Ref. 17, and ~10 cm^{-1} for other levels. Additionally, some symmetry assignments have been changed (levels 37, 38, 40–42, 45), so that the values are then in agreement with the present study except for the systematic calibration differences. For comparison, the energy levels from this study of the 10 K absorption spectrum of $Cs_2NaY_{0.9}Nd_{0.1}Cl_6$ are also listed in the table. Only the stronger transitions were observed and much of the ultraviolet region was obscured by the interconfigurational absorption and emission transitions of Pr^{3+} impurity.

The energy levels derived from the 20 K luminescence spectrum of $Cs_2NaGdCl_6:Nd^{3+}$ are listed in Table II and are in agreement with the data for the other hosts. The levels from the 30 K excitation spectrum[19] are also included and the spectral data have been reinvestigated. From the revised analysis, first, the $^2H(2)_{9/2}\Gamma_6, a\Gamma_8$ levels at 12 528, 12 536 cm^{-1} have been reassigned at 12 411, 12 528 cm^{-1}, respectively. Second, the two levels at 13 413 cm^{-1} have been reassigned at 13 413 cm^{-1} and tentatively at 13 422 cm^{-1}. Third, the tentative assignment at 19 645 cm^{-1} has been deleted. In addition, the 10 K absorption spectrum of $Cs_2NaGd_{0.93}Nd_{0.07}Cl_6$ has been investigated up to 30 000 cm^{-1} and the derived levels are also listed in Table II.

V. CRYSTAL FIELD CALCULATIONS

The 98 measured energy levels were fitted to the standard model Hamiltonian[40–43] involving a total of 18 parameters. These comprise 16 free ion parameters, out of which E_{ave} tunes the mean energy and the remaining 15 control the term multiplets: the Slater parameters $F^k(k=2,4,6)$, the configuration interaction parameters α, β, γ, the three body parameters $T^i(i=2,3,4,6,7,8)$; the parameters of magnetic interactions M^k $(k=0(2,4); M^2=0.56M^0; M^4=0.38\ M^0)$ and P^k $(k=2(4,6); P^4=0.75P^2; P^6=0.5\ P^2)$; and the spin-orbit coupling constant, ζ, which controls the interaction between *SLJ* levels. Two more parameters are required to account for the crystal field interaction in octahedral symmetry: B_0^4 and B_0^6. The Wybourne spherical tensorial notation is adopted herein, and in the cubic environment, $B_4^4=\pm B_0^4(5/14)^{1/2}$ and $B_4^6=\mp B_0^6(7/2)^{1/2}$.

The $4f^3$ configuration comprises the same 17 terms as $4f^{11\ 30}\ ^4S$, ^4D, ^4F, ^4G, ^4I, ^2P, $^2D(1,2)$, $^2F(1,2)$, $^2G(1,2)$, $^2H(1,2)$, ^2I, ^2K, ^2L. The 98 experimentally observed levels belong to the 15 terms: quartets ^4I, ^4F, ^4S, ^4D, ^4G and doublets $^2H(1,2)$, $^2G(1)$, ^2K, ^2P, $^2D(1,2)$, ^2I, $^2F(2)$, and ^2L. The parameters $F^k(k=2,4,6)$, α, β, $T^i(i=3,4,6,7)$, M^0, ζ, B_0^4, and B_0^6 were all varied in turn, starting from values determined with smaller datasets.[19] The best fit, with a mean deviation of 32 cm^{-1} between the 98 experimental and calculated energy levels, is listed in Table III (calc. *E*1) and the corresponding energy parameters are given in Table IV (in column *E*1).

Separate fits were made to the quartet levels (which predominate at lower energy), and to the doublet levels, by varying the fourth and sixth degree crystal field parameters alone. It turns out that the mean deviation for the 51 quartet states is equal to 28.4 cm^{-1} and that for the 47 doublet states is 35.1 cm^{-1}. While the overall fourth degree crystal field parameter is fitted as 1987 cm^{-1}, it is equal to 2018 and 1970 cm^{-1} for the doublet and quartet fits, respectively, that is 2.4% greater in the former case. This is far from the situation of Tm^{3+} in $TmCl_6^{3-}$ where the difference in fitting singlet and triplet states was 60%.

TABLE IV. Empirical hamiltonian parameters of Nd^{3+} in $Cs_2NaNdCl_6$.

Parameter	Calc. *E*1[a]	Calc. *E*2[b]
F^2	71106	71290
F^4	51440	51815
F^6	35068	35128
α	21.29	21.27
β	−641	−662
γ	1654	1671
T^2	375	364
T^3	42	43
T^4	66	62
T^6	−279	−303
T^7	373	377
T^8	285	329
M^0	1.99	1.84
P^2	158	145
$\zeta(4f)$	880	882
$B_0^4(4f4f)$	1987	3180
$B_0^6(4f4f)$	257	573
$E'_{ave}-E_{ave}$		[140000]
X		1.23
$\zeta(np)$		[4100]
$B_0^4(4fnp)$		28533
N	98	98
n_p	18	20
σ	31.9	12.9

[a]Calc. *E*1: normal fit with 98 levels.

[b]Calc. *E*2: CIACF calculation. Parameters in square brackets were varied by steps and then held constant during the refinement of the other parameters.

The $^2H(2)$ multiplet of the $4f^3$ and $4f^{11}$ configurations belongs to a set of "abnormal" terms existing among the series of rare earth ions, for which the crystal field levels can seldom be satisfactorily fitted by the standard procedure.[44] This fact is particularly conspicuous for Nd^{3+}[45] and well observed for the isolated and rather pure $^2H(2)_{11/2}$ level. For $Cs_2NaNdCl_6$, the experimental and calculated $^2H(2)_{11/2}$ splittings are equal to 189 and 58 cm^{-1}, respectively. To match the experimental splitting would require a nonrealistic B_0^4 value higher than 4500 cm^{-1}. The mean deviation Δ within $^2H(2)_{11/2}$ amounts to 71 cm^{-1} while a global fit excluding the four $^2H(2)_{11/2}$ levels gives $\Delta=29.5$ cm^{-1}. It has been shown[45,46] for the case of Nd^{3+} that

the discrepancy is connected with the strength of the fourth order crystal field (defined in Table V). This is visible in Fig. 4 which represents the ratio of calculated over experimental $^2H(2)_{11/2}$ splittings versus the ratio $S^4/[(S^2)^2+(S^6)^2]^{1/2}$ for 32 compounds. The discrepancy can be fairly well corrected by an empirical modification of the $\langle^2H(2)\|U^4\|^2H(2)\rangle$ reduced matrix element. A crystal field analysis for a series of ten Nd^{3+} systems showed that the best multiplying factor for the correction was close to 0.25.[46] In other words, $\langle^2H(2)\|U^4\|^2H(2)\rangle$ is replaced by $(1-0.75)\times\langle^2H(2)\|U^4\|^2H(2)\rangle$. The same kind of discrepancy is observed for Er^{3+} where the empirical correction is close to $(-1-0.75)\langle^2H(2)\|U^4\|^2H(2)\rangle$. That suggested it was due to a two particle interaction whose sign does not change in the second half of the lanthanide series. It turned out after the development of the correlation crystal field[47] that the correction had approximately the same effect as the $g^4_{10,A}$ operator of the correlation crystal field (CCF). The correction is efficient for $^2H(2)_{11/2}$ and $^2H(2)_{9/2}$ and for those levels which are coupled to them by spin-orbit interaction, such as $^4I_{9/2}$, $^4F_{9/2}$, and $^4G_{11/2}$. The empirical correction is easy to apply since it suffices to replace the value of $\langle^2H(2)\|U^4\|^2H(2)\rangle=0.495$ in Nielson and Koster's tables[48] by 0.124 for Nd^{3+} and 0.866 for Er^{3+}.[49]. Some other crystal-field "bugs" are referred to in Ref. 50. Concerning Nd^{3+}, the above correction was applied in the parametric simulation of energy levels of in Nd_2O_2S, $LiYF_4$, NdOCl, Nd_2O_3, and Y_2O_3,[46,51] with substantial improvements of the mean deviation. If that correction is applied to $NdCl_6^{3-}$, the parameters do not change much. The mean deviation within $^2H(2)_{11/2}$ falls down to 5 cm^{-1} but the global deviation (28.5 cm^{-1}) is only slightly improved with respect to the normal fitting (32.5 cm^{-1}). It is noteworthy that on average, the levels other than $^2H(2)_{11/2}$ are also slightly improved. For large data sets, the "weight" of the $^2H(2)$ levels is relatively less important and the higher levels are practically unchanged with respect to the $4f^3$ calculation. That explains the rather small influence on the global performance.

A more elegant improvement of the energy level fitting involves the inclusion of the configuration interaction with excited configurations. The discussion of the relevant types of configurations has been given previously[52,53] and the scope is limited to those of the type $4f^{N-1}np$ and $4f^{N+1}mp^5$ in the present case of a centrosymmetric system. For Pr^{3+} in $Cs_2NaPrCl_6$,[29] the interaction was assumed to occur between $4f^2$ and $4fnp$. By analogy, in the present case, the interaction is switched on between $4f^3$ and $4f^2np$. The excited configuration contains the 27 terms ^2S, $^2P(1,2,3)$, $^2D(1,2,3)$, $^2F(1,2,3)$, $^2G(1,2,3)$, $^2H(1,2,3)$, $^2I(1,2)$, ^2K, ^4S, ^4P, $^4D(1,2)$, ^4F, $^4G(1,2)$, and ^4H. The additional parameters necessary for the description of the excited configuration $4f^2np$ and its interaction with $4f^3$, are (i) the mean energy of the excited configuration with respect to $4f^3$ (ii) the interconfiguration parameters R^k (among the latter, only the hybrid integrals $R^2(f,f,f,p)$ and $R^4(f,f,f,p)$ are relevant); (iii) the spin-orbit coupling constant $\zeta(np)$; and (iv) the crystal field parameter $B^4_0(4fnp)$. For Pr^{3+} in $Cs_2NaPrCl_6$, it was assumed that np was actually $6p$, i.e., a metal orbital. Thus, in the present case, the starting values for the interconfiguration parameters were chosen according to the same hypothesis. The atomic quantities (i), (ii), (iii) above, calculated by Cowan's program[54] are (in cm^{-1}): (i) $E'_{ave}-E_{ave}=140\,000$ cm^{-1}; (ii) $R^2(f,f,f,p)=-4680$, $R^4(f,f,f,p)=-2785$; and (iii) $\zeta(6p)=4100$. $E'_{ave}-E_{ave}$ and $\zeta(6p)$ were kept fixed. We chose to fit a unique common multiplier X for the R^k's, which was set equal to 1 at the start of the fit. As for the crystal field parameter $B^4_0(4f5p)$, we expected a value of the order of $B^4_0(4f4f)$ scaled by the ratio of the radial integrals: $r^4(4f5p)/r^4(4f4f)=3.19$. However, it was stated for $Cs_2NaPrCl_6$ that the final fitted $B^4_0(4f6p)$ value was about ten times that of $B^4_0(4f4f)$. In the standard analysis above, the fitted value of $B^4_0(4f4f)$ was 1987 cm^{-1}, hence by analogy, a starting value $B^4_0(4f6p)=20\,000$ cm^{-1} was adopted. The total number of parameters in the multiconfiguration analysis then amounts to 20 (versus 18 parameters for the analysis of $4f^3$ alone). All the parameters were varied in turn and the mean deviation decreased quickly down to 12.9 cm^{-1}. Therefore, the inclusion of two more parameters, [$B^4_0(4f6p)$ and X], than in the standard procedure, reduces the deviation by a factor of 2.5. The parameter values are listed in Table IV (in column $E2$). We note that the free-ion parameters are very similar in columns $E1$ and $E2$. Besides, the crystal field parameters $B^4_0(4f4f)$ and $B^6_0(4f4f)$ are 1.6 and 2.2 larger than in the standard analysis. $B^4_0(4f6p)$ is, as inferred from the earlier work on Pr^{3+}, about ten times larger than $B^4_0(4f4f)$. All three parameters are very similar to those fitted previously for $Pr^{3+}(4f^2)$ in $PrCl_6^{3-}$.[29] We shall rely on the final values of the fitted parameters to confirm the physical mechanism.

One effect of covalency in rare earth compounds is a displacement of the lines of their absorption spectra (nephelauxetic effect). This is reflected in the standard theory by a variation of the $4f^3$ Slater integrals. Indeed for what concerns the free-ion parameters, the effects of covalency are absorbed by the variations of F^2, F^4, and F^6 (coefficients of two-electron operators) and those parameters do not change much herein when configuration interaction is introduced. On the contrary, the crystal field parameters (coefficients of one-electron parameters) and notably the strength of the fourth order crystal field, S^4, fully feel the effects of configuration interaction and might be tools for the evaluation of covalency of a compound. The values of S^4 are discussed in Sec. VII and listed in Table V.

VI. DISCUSSION

It is attractive to seek a unique physical interpretation for the efficient improvement of the crystal field analysis for the four chloroelpasolite systems examined up to now: for Pr^{3+}, Nd^{3+}, Er^{3+}, and Tm^{3+} (for f^N, $N=2$, 3, 11, and 12, respectively). For that goal, we confine ourselves to the considerations of the final fitted parameters for the p electron and of the configuration involving the $4f$ and the p-electrons.

A. Pr^{3+} and Nd^{3+}

For Pr^{3+} (Ref. 29) and Nd^{3+} in the first half of the lanthanide series, we have utilized the exact $\zeta(p)$ value deliv-

TABLE V. Fourth and sixth-order crystal field strength, S^k (in cm^{-1}), from various energy level fits for Nd^{3+} in crystals.

Nd^{3+} system	Ref.	Site sym.	$N(\sigma)$[a]	N_{par}[b]	S^{2c}	S^{4c}	S^{6c}	RSC[d]	S^6/S^4	$\Delta_{calc}/\Delta_{exp}$[e]
K_2YF_5	10	C_{2v}	76(19)	9	162	322	199	1.25	0.62	0.38
$LiYF_4$	8	D_{2d}	129(24,*24*)	6(*7*)	88	278	204	1.25	0.73	0.41
BaY_2F_3	8	C_{2v}	91(20,*17*)	9(*12*)	154	248	235	0.88	0.95	0.42
LaF_3	71	C_{2v}	146(14)	9	61	170	252	0.66	1.48	0.66
NdF_3	62	C_{2v}	116(14)	9	75	154	277	0.54	1.80	0.66
Cs_2NaYCl_6	17	O_h	34(–)	2	0	396	98	4.04	0.25	[f]
$Cs_2NaGdCl_6$	19	O_h	41(15)	2	0	361	92	3.92	0.25	[f]
$Cs_2NaNdCl_6$	this work	O_h	98(32,13)	2(3)	0	515	170	3.03	0.33	0.31
$[(C_6H_5)_3PH]_3NdCl_6$	58	O_h	31(20)	2	0	321	160	2.01	0.50	0.86
RbY_2Cl_7	11	C_{2v}	156(15,*10*)	9(*12*)	103	214	82	1.63	0.39	0.99
RbY_2Cl_7	11	C_{2v}	151(18,*11*)	9(*12*)	84	225	113	1.60	0.50	1.02
$LaCl_3$	14	C_{3h}	101(8)	4	38	48	129	0.36	2.69	0.92
$LaCl_3$	8	D_{3h}	128(9,*8*)	6(*7*)	35	45	132	0.36	2.93	0.83
$YAl_3(BO_3)_4$	56	D_3	20(9)	6	79	278	53	2.92	0.19	[f]
Nd_2O_2S	59	C_{3v}	96	6	39	224	94	2.20	0.42	0.27[g]
$NdAl_3(BO_3)_4$	1	D_3	135(14)	6	104	287	116	1.84	0.40	0.86
$NdAl_3(BO_3)_4$	1	C_2	135(15)	14	108	286	118	1.79	0.41	0.86
$NdVO_4$	8	D_{2d}	71(18,*17*)	6(*7*)	9	236	144	1.64	0.61	0.30
$YAsO_4$	70	D_{2d}	102(15)	5	38	218	140	1.50	0.64	0.30
$Nd_2Te_4O_{11}$	8	C_s	103(18,*13*)	14(*17*)	105	248	129	1.49	0.52	0.33
YVO_4	70	D_{2d}	96(16)	5	46	245	167	1.41	0.68	0.34
$NdH[O_3P(CH_2)_3PO_3]$	4	C_{2v}	67(17)	9	79	280	185	1.39	0.66	[f]
YVO_4	6	D_{2d}	11(-)	5	36	233	167	1.36	0.72	[f]
$Y_3Al_5O_{12}$	68	D_2	144(31,*15*)	9(*12*)	110	484	343	1.34	0.71	0.44
A-Nd_2O_3	63	C_{3v}	90(27)	6	177	340	194	1.29	0.57	0.35
Y_2O_3	51 and 69	C_2	72(21)	27	300	465	202	1.29	0.43	0.52
$Nd_3Ga_5O_{12}$	15	D_2	104(16,*15*)	9(*18*)	107	413	308	1.27	0.75	0.65
YPO_4	70	D_{2d}	90(16)	5	55	203	160	1.20	0.79	0.30
$Y_3Al_5O_{12}$	9	D_2	106(18)	9	167	533	444	1.12	0.83	0.47
$SrWO_4$	5	S_4	70(11)	5	132	199	154	0.98	0.77	0.93
$Na_3[$ NdODA$)_3]\cdot 2NaClO_4\cdot 6H_2O$	66	D_3	116(14)	6	9	218	248	0.88	1.14	0.59
$LaVO_4$	8	C_{2v}	74(17,*16*)	9(*12*)	187	209	191	0.78	0.91	0.71
$NdPO_4$	8	C_{2v}	90(18,*17*)	9(*12*)	147	190	224	0.71	1.18	0.64
NdP_5O_{14}	57	C_s	60(7)	14	197	162	123	0.70	0.76	0.58
$LuAlO_3$	60	C_s	98(12)	15	200	261	318	0.69	1.22	0.82
NdOCl	61	C_{4v}	105(20)	5	212	171	131	0.69	0.77	0.64
$LuAlO_3$	8	C_s	106(13,*11*)	14(*17*)	212	259	326	0.67	1.26	0.73
$YAlO_3$	8	C_s	96(14,*12*)	14(*17*)	187	256	333	0.67	1.30	0.69
$NdAlO_3$	64	D_3	116(9,*9*)	6(*12*)	106	115	356	0.31	3.10	0.82
$Sr_5(PO_4)_3F$	7	C_s	52(7)	14	636	349	176	0.53	0.50	[f]
$[Nd(H_2O)_9](CF_3SO_3)_3$	13	C_{3h}	79(12,*9*)	4(*8*)	31	85	163	0.51	1.92	0.44

TABLE V. (*Continued.*)

Nd^{3+} system	Ref.	Site sym.	$N(\sigma)$[a]	N_{par}[b]	S^{2c}	S^{4c}	S^{6c}	RSC[d]	S^6/S^4	$\Delta_{calc}/\Delta_{exp}$[e]
$Nd(C_2H_5SO_4)_3\cdot 9H_2O$	15	D_{3h}	61(9,*8*)	6(*12*)	35	82	162	0.49	1.98	[f]
$Ca_5(PO_4)_3F$	7	C_s	59(8)	14	608	303	171	0.48	0.56	[f]
$Nd(NO_3)_3\cdot 6H_2O$	67	C_{3v}	98(22)	6	51	118	250	0.46	2.11	0.98
$Nd(C_2H_5SO_4)_3\cdot 9H_2O$	65	C_{3h}	47(9,*5*)	4(*8*)	29	76	161	0.46	2.12	0.57

[a]$N(\sigma)$ number of crystal field levels fitted and reported rms standard deviation or mean deviation in parentheses. When two values of σ are given, the second refers to CCF (or CIACF).

[b]N_{par} number of crystal field parameters employed in the fits for the values of σ. Values in italics in the columns $N(\sigma)$ and N_{par} refer to a correlation crystal field calculation.

[c]$S^k=\left(7/(2k+1)\begin{pmatrix}3 & 3 & k\\ 0 & 0 & 0\end{pmatrix}^2 \sum_{q=-k,k}(B_q^k)^2\right)^{1/2}$.

[d]Relative strength of the fourth order crystal field: $S^4/[(S^2)^2+(S^6)^2]^{1/2}$.

[e]Calculated versus experimental splitting of the $^2H(2)_{11/2}$ multiplet.

[f]$^2H(2)_{11/2}$ level set not reported or incomplete.

[g]0.99 when $\langle {}^2H(2)\|U^4\|{}^2H(2)\rangle$ is divided by 4.

ered by Cowan's interaction program[54] for a p electron in $4f^{N-1}6p$ (3877 and 4100 cm^{-1}, respectively). The gaps between the ground and excited configurations were set equal to the theoretical values (124 000 and 140 000 cm^{-1} respectively). The theoretical $R^k(f,f,f,p)$ parameters, equal to −6450 and −4433 cm^{-1} ($k=2$ and 4, respectively) for Pr^{3+}; −4680 and −2785 cm^{-1} ($k=2$ and 4, respectively) for Nd^{3+}, were utilized in the calculation. At the outset, the fitted multipliers X were equal to 1.39 (a mean value for $k=2$ and 4) and 1.23 for Pr^{3+} and Nd^{3+}, respectively. Thus there seems to be no possible hesitation and the hypothesis of a $4f^N \rightarrow 4f^{N-1}6p$ interaction seems well accredited for both systems. If the energy of the excited configuration is lowered, X increases as well as $B_0^4(f,p)$ but the mean deviation remains nearly constant down to 50 000 cm^{-1}. For example, for $E'_{ave}-E_{ave}=57\,600$ cm^{-1}, the mean deviation is equal to 13.4 cm^{-1}, and for $E'_{ave}-E_{ave}=124\,000$ cm^{-1} it is 12.9 cm^{-1}.

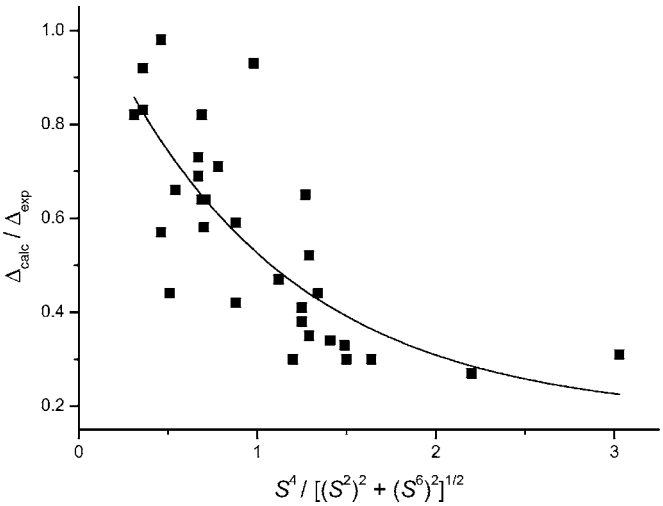

FIG. 4. The ratio of calculated over experimental $^2H(2)_{11/2}$ splittings versus the ratio $S^4/[(S^2)^2+(S^6)^2]^{1/2}$ for 32 compounds. The exponential line fit is drawn as a guide to the eye.

B. Er^{3+} and Tm^{3+}

When the reflected configurations Er^{3+30} and Tm^{3+31} are considered, the interaction which is efficient in reducing discrepancies is $4f^N mp^6 \rightarrow 4f^{N+1}mp^5$. That ruins the hope for an unique interpretation on both sides of the half-filled lanthanide shell. The result can be interpreted in two different ways; either a process involving the core $5p$ electrons: $4f^N5p^6 \rightarrow 4f^{N+1}5p^5$, or one involving the ligand $3p$ electrons: $4f^N3p^6 \rightarrow 4f^{N+1}3p^5$. The practical difference between the two processes is manifested in the characteristics of the p electron. In the first case, $\zeta(p)$, $R^k(f,f,f,p)$ and the gap are up to five times larger than in the second one. The first process was identified as responsible in the case of $LuVO_4$, $LuPO_4$, and $LaOBr:Tm^{3+}$. However for Tm^{3+} in $Cs_2NaTmCl_6$ and Er^{3+} in $Cs_2NaErCl_6$, no improvement could be obtained with the large theoretical values of $\zeta(p)$ and $R^k(f,f,f,p)$. When $\zeta(p)$ and $R^k(f,f,f,p)$ were lowered, the gap also decreased strongly, making us suspect that the ligand p electrons were involved in the interacting process. The $4f^N3p^6 \rightarrow 4f^{N+1}3p^5$ interactions were therefore interpreted as the preferred mechanism for the improvement of the crystal field calculation. We showed that the calculation could be carried out since a non-negligible part of the orbital moment of the ligand $3p$ electrons are projected on the coordinate system of the central ion as p orbitals.[30]

We then had to admit for the chloro-elpasolites that a different configuration interaction process occurs in each half of the lanthanide series: a transfer from the f^N orbital towards the empty $6p$ orbital in the first half, but a transfer from the ligand electrons towards f^N in the second half.

VII. COMPARISON WITH OTHER STUDIES

It is instructive to compare the results from the crystal field calculations of the present study with those for other solid-state Nd^{3+} materials from the literature. Table V summarizes the results for these systems and the compounds have been arranged according to the ligands: F, Cl, and O.

Columns 1–5 specify the compound, the reference number, the site symmetry at the rare earth site, the number of levels considered and the mean deviation obtained in the crystal-field fitting, whether a standard or nonstandard (CIACF, CCF analysis) fitting has been performed, and the number of crystal field parameters utilized. Rather than the global crystal field strength S, we have found it more meaningful to decompose it into its components S^2, S^4, and S^6, the origin and the influence of which are different. They are listed in columns 6–8. In column 9 (RSC) are reported the relative strengths of the fourth order crystal field, $S^4/[(S^2)^2+(S^6)^2]^{1/2}$ and in column 10 the ratio S^6/S^4 is given. Within each category (fluorides, chlorides, oxides) the compounds are listed according to a decreasing order of RSC. Although different studies on the same compound exhibit some variations, they globally agree within the main features. Ethylsulfate and doped lanthanum chloride are at the end of the list, while the elpasolites display the largest values.

The parameter S^2 is essentially of electrostatic origin. Individual contributions to B_0^2 cancel whenever $3\cos^2\theta-1=0$, with θ being the polar angle of a particular ligand. The fourth order crystal field strength, S^4 has a mixed electrostatic and covalent origin. There is no simple relationship between S^4 and the ligand type, so that clearly other factors such as coordination number, geometry and bond length are important. The most extreme values of S^4 are found within the set of compounds with chloride ligands: 515 and 45 cm^{-1} for $Cs_2NaNdCl_6$ and $LaCl_3$, respectively. The values of B_0^4 can be simulated by the covalo-electrostatic model which assumes that the parameter is the sum of a well shielded electrostatic contribution and a covalent contribution mainly due to kinetic energy.[55] The values predicted for B_0^4 are 3144 and -496 cm^{-1} for the elpasolite and the chloride respectively while the experimental values are 1987 and -340 cm^{-1}. This large difference which places the elpasolite and the chloride, respectively at the forefront and at the end of the list in Table V, can be crudely explained in the following way, considering only the covalent contribution: the calculated crystal field parameters are related to the square of the kinetic energy interaction. It is evaluated by a sum of overlaps which decrease rapidly when the rare earth-ligand distance increases. It is equal to 4×10^{-5} and 1×10^{-5} cm^{-1} for one Nd-Cl pair in the elpasolite and chloride, respectively. The six rare earth-ligand distances are equal to 2.68 Å in $Cs_2NaNdCl_6$ and the nine Nd-Cl distances in the chloride are approximately 2.95 Å in $LaCl_3$. The kinetic energy value has to be multiplied by a sum of the C_q^k's over the ligands' sites. This sum amounts to 3.5 in the elpasolite $(4\times0.375+2)$ where all six contributions are positive, and $-1.07(3\times0.375-6\times0.365)$ in the chloride where there is a partial cancellation. The expected ratio of $B_0^4(Cs_2NaNdCl_6)/B_0^4(LaCl_3)$ is then approximately $4\times3.5/(1\times1.07)\approx13$ which is not far from the experimental S^4 ratio which is equal to 11.4. The differences of S^4 between the three elpasolite compounds $Cs_2NaLnCl_6$ with Ln=Nd,Gd,Y are attributed to the use of different energy level datasets and number of levels fitted. In these cases concerning the elpasolite structure, the neighbors up to the fourth-nearest from Ln^{3+} are identical: the first-nearest are 6 Cl^- at 2.68 Å; the second-nearest are 8 Cs^+ at 4.73 Å; the third-nearest are 6 Na^+ at 5.46 Å; and the fourth-nearest are 24 Cl^- at 6.12 Å. Only the remote fifth-nearest neighbors (Nd, Gd, or Y) at 7.7 Å are different. One can also suspect the band gap between $Nd^{3+}(4f^3)$ and the Cl^- ligands $(3p^6)$ to be different in the three compounds.

B_0^6 is essentially due to covalency. Among the oxides, most of the S^6/S^4 values range from 0.4 to 0.7. Some compounds display higher values of this ratio, as the garnets: $Y_3Al_5O_{12}$(0.8), $Nd_3Ga_5O_{12}$(0.75); the perovskites: $LuAlO_3$(1.25), $YAlO_3$(1.3), $NdAlO_3$(3.10); and $LaCl_3$(2.93), NdODA (1.14), $LaVO_4$(0.91), NdF_3(1.8), neodymium nitrate (2.11) and ethylsulfate (2.12). The case of $LaCl_3$ was discussed above. More generally, the high values of S^6/S^4 are the result of two effects: the first one is due to the geometry of the ligand shell and occurs for high coordination numbers. For instance in $NdAlO_3$ (coordination number, CN=12) or as already mentioned for $LaCl_3$ (CN=9) the contributions to B_0^4 nearly cancel each other. The second cause is a second-neighbor effect.[72] The presence of Al^{3+} or Ga^{3+} as a second neighbor has the effect of increasing B_0^6 to the detriment of B_0^4 and hence gives a large S^6/S^4 ratio. $NdAlO_3$ displays the largest value due to the combination of both effects. A satisfying simulation of the 6 crystal field parameters of $NdAlO_3$ requires the Nd^{3+} $(4f)$, oxygen $(2p)$, and aluminum $(2p)$ orbitals to be taken into account.

Table V also lists the ratio of the calculated (using the standard $4f^3$ program) versus experimental $^2H(2)_{11/2}$ splitting $(\Delta_{calc}/\Delta_{exp})$, whilst Fig. 4 represents these values as a function of the relative strength parameter. Despite an evident scatter of the experimental points, the obvious trend is a pronounced nonlinear variation of the discrepancy with the RSC parameter. The compounds which are present on the lowest part of the curve are the elpasolites, the borate $YAl_3(BO_3)_4$, and Nd_2O_2S. On the highest part of the curve are those systems for which the ratio $(\Delta_{calc}/\Delta_{exp})$ approaches 1, i.e., those quoted above with high S^6/S^4 values.

Calculations for $NdCl_6^{3-}$ were performed in three previous studies. They were mostly limited to the spectral region below 21 000 cm^{-1}, with assignments for 33, 34, and 41 energy levels, and with those for $^2H(2)_{11/2}$ missing for Nd^{3+} in the cubic hosts Cs_2NaYCl_6 (Ref. 17) and $Cs_2NaGdCl_6$.[19] Calculations for other systems employed literature data and it is sometimes unclear exactly which energy levels were employed in the parametrizations.[8,15] In some other studies [Nd^{3+} in $YAl_3(BO_3)_4$ (Ref. 56) and in $NdAl_3(BO_3)_4$ (Refs. 1 and 2)] the energy level assignments differ considerably. Correlation crystal field analyses have been performed for some of the systems in Table V, employing between one to six additional crystal field parameters but generally, except for $Y_3Al_5O_{12}:Nd^{3+}$ (Ref. 68) and $RbY_2Cl_7:Nd^{3+}$,[11] the improvements to the datafits have been small. The fitting errors in some of the systems listed in Table V are given as <10 cm^{-1}, but in many cases only lower energy levels have been included in the fitting and the anomalous $^2H(2)_{11/2}$ levels have been omitted (compare this with the first 30 levels in Table III where the errors are <10 cm^{-1} in the CIACF fit). The most comprehensive fits are those of 144 Nd^{3+} levels in $Y_3Al_5O_{12}$[68] utilizing 9 or 12 crystal field parameters, and of

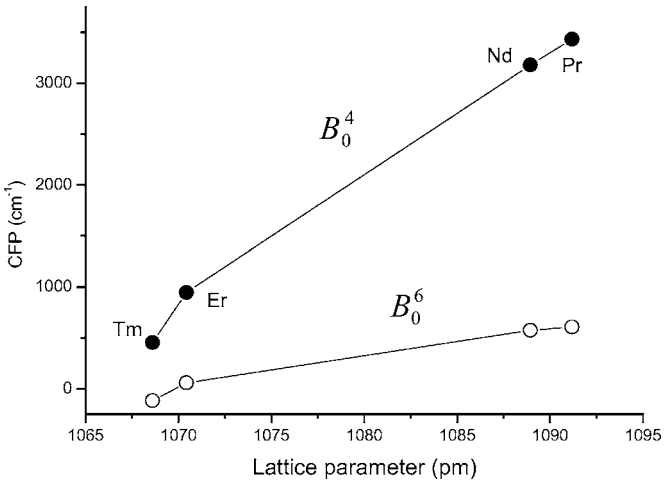

FIG. 5. Plot of $4f$ electron crystal field parameters from CIACF parametrizations against lattice parameter for $Cs_2NaLnCl_6$ (Ln =Pr,Nd,Er,Tm). The lines are a guide to the eye.

Nd^{3+} at two different $C_{3\nu}$ sites in RbY_2Cl_7, where over 150 Kramers doublets were fitted utilizing these same numbers of parameters.[11]

The free ion parameters show a considerable range of values for the fittings of systems in Table V. There are no clear (nephelauxetic) trends for oxide, fluoride and chloride hosts. The Slater parameters show the ranges (in cm^{-1}): F^2(68 865–73 137); F^4(48 107–54 501); F^6(32 008–36 930), with the upper values in each case being those for $Nd(NO_3)_3 \cdot 6H_2O$ whilst the lower ones refer to A-type Nd_2O_3.[15] A subsequent barycenter fitting for A-type Nd_2O_3 gave rather higher Slater parameter values.[12] The upper and lower values for $\zeta(4f)$ are 883 cm^{-1} [in $SrWO_4$ (Ref. 5) and NdF_3 (Ref. 8)] and 866 cm^{-1} in $Nd_3Ga_5O_{12}$.[15] Values of α, β, γ show wide ranges (in cm^{-1}): α [0.56 (Ref. 17) to 30.8 (Ref. 12)]; β [−513 (Refs. 8 and 10) to −684 (Ref. 8)] and γ [750 (Ref. 4) to 2592 (Ref. 15)]. The ranges of the three-body parameter T^2 and the magnetic interaction parameters M^0, P^2 are (in cm^{-1}): T^2 [154 (Ref. 10) to 749 (Ref. 8)]; M^0 [0.14 (Ref. 8) to 2.43 (Ref. 8)]; and P^2 [58 (Ref. 15) to 319 (Ref. 8)]. The wide variations of the atomic parameters are due to the different fitting procedures and numbers of levels employed, and most likely show that the extreme values arise because the crystal field parameters are not fitting the data well, rather than that systematic covalency or nephelauxetic effects occur.

The elpasolite systems comprise the only cases in Table V where the $4f^3$ and $4f^25d$ configurations are unmixed by odd terms in the crystal field. Figure 5 shows the variations of the B_0^4 and B_0^6 crystal field parameters from the CIACF fits for $Ln^{3+}=Pr^{3+}$,[29] Nd^{3+}, Er^{3+},[30] and Tm^{3+} (Ref. 31) in $Cs_2NaLnCl_6$ against the lattice parameter. Plots of the fourth and sixth degree crystal field parameters deduced from energy level fittings using one-electron crystal field parameters with the exclusion of configuration interaction have recently been given.[24] In that case a decrease in the parameter values was found when traversing from Ce^{3+} to Yb^{3+}. The radial integrals which are incorporated into crystal field parameters show a decrease across this series. It is interesting that the plot in Fig. 5 shows the same trend but with rather different values of the crystal field parameters.

VIII. CONCLUSIONS

This work has provided a relatively complete analysis of the Nd^{3+} ion in the neat hexachloroelpasolite lattice, for comparison with three other elpasolite systems studied previously. The region of absorption measurements was from 400 to 40 000 cm^{-1} and the luminescence spectra span the range from 7950 up to 27 800 cm^{-1}. The main conclusions are itemized below.

(1) The $Cs_2NaNdCl_6$ elpasolite is an ideal system for studying the $4f^3$ energy level system because the nearly octahedral Nd^{3+} site symmetry gives rise to high crystal field level degeneracies, the selection rules are restrictive, vibronic fingerprints aid spectral assignments, the crystal field interactions are strictly modeled by only two parameters, and configuration mixing only occurs with equiparity configurations.

(2) The ZPL and vibronic sidebands in the spectra are well resolved and have been comprehensively assigned. The observed optical spectral lines and the corresponding assignments are consistent with those of the Nd^{3+} ion diluted into $Cs_2NaGdCl_6$ and Cs_2NaYCl_6. Analyses of the emission spectra from the $^4F_J(J=3/2,5/2)$, $^4G_{7/2}$, and $^4D_{3/2}$ luminescent states serve to substantiate the assignments from the absorption spectra.

(3) Eighty six crystal field levels have been firmly assigned plus a further 12 tentatively assigned levels, altogether spanning 34 $^{2S+1}L_J$ multiplet terms.

(4) Analysis of the $4f^3$ energy level dataset is vastly improved through the inclusion of the configuration interaction (CI) of $4f^3$ with $4f^26p$.

(5) The CI is of the type $4f^3/4f^2np$. This result differs from the CI for Ln=Tm,Er in $Cs_2NaLnCl_6$, where the interacting configuration is of the charge-transfer type: $4f^N/4f^{N+1}3p^5$.

(6) Comparison with other solid-state studies of Nd^{3+} shows a nonlinear relationship of the discrepancy in the calculated versus the experimental splitting of the $^2H(2)_{11/2}$ multiplet as a function of the relative strength of the fourth order crystal field parameter.

(7) The derived $4f^3$ parameter values for other Nd^{3+} systems show considerable scatter. This is notable for the scalar CI parameters, where for example, the fitted value of α varies by a factor of 50.

(8) Although the fitted values for the fourth- and sixth-order crystal field parameters from the CI-assisted crystal field fit are rather greater than from the $4f^3$ fit in the present case, the trend for the four systems studied so far (Ln =Pr,Nd,Er,Tm) shows that there is a decrease in magnitude for both crystal field parameters across the Ln^{3+} series.

ACKNOWLEDGMENT

Financial support for this study under the Hong Kong Research Grants Council Earmarked Grant City 102304 is gratefully acknowledged.

[1] C. Cascales, C. Zaldo, U. Caldiño, J. García Solé, and Z. D. Luo, J. Phys.: Condens. Matter **13**, 8071 (2001).
[2] D. Jaque, O. Enguita, U. Caldiño, M. O. Ramirez, J. García Solé, C. Zaldo, J. E. Muñoz-Santiuste, A. D. Jiang, and Z. D. Luo, J. Appl. Phys. **90**, 561 (2001).
[3] J. Derouet, L. Beaury, and P. Porcher, J. Alloys Compd. **323-324**, 460 (2001).
[4] E. Antic-Fidancev, F. Serpaggi, and G. Férey, J. Alloys Compd. **319**, 140 (2001).
[5] F. Cornacchia, A. Toncelli, M. Tonelli, E. Cavalli, E. Bovero, and N. Magnani, J. Phys.: Condens. Matter **16**, 6867 (2004).
[6] F. J. Manjón, S. Jandl, G. Riou, B. Ferrand, and K. Syassen, Phys. Rev. B **69**, 165121 (2004).
[7] J. B. Gruber, C. A. Morrison, M. D. Seltzer, A. O. Wright, M. P. Nadler, T. H. Allik, J. A. Hutchinson, and B. T. Chai, J. Appl. Phys. **79**, 1746 (1996).
[8] E. Rukmini, C. K. Jayasankar, and M. F. Reid, J. Phys.: Condens. Matter **6**, 5919 (1994).
[9] J. B. Gruber, D. K. Sardar, R. M. Yow, T. H. Allik, and B. Zandi, J. Appl. Phys. **96**, 3050 (2004).
[10] M. Yin, Y. Li, N. Dong, V. N. Makhov, N. M. Khaidukov, and J. C. Krupa, J. Alloys Compd. **353**, 95 (2003).
[11] M. Karbowiak, N. M. Edelstein, J. Drozdzyński, and K. Kossowski, Chem. Phys. **277**, 361 (2002).
[12] E. Rukmini and C. K. Jayasankar, Physica B **212**, 167 (1995).
[13] J. R. Quagliano, G. W. Burdick, D. P. Glover-Fischer, and F. S. Richardson, Chem. Phys. **201**, 321 (1995).
[14] H. M. Crosswhite, H. Crosswhite, F. W. Kaseta, and R. Sarup, J. Chem. Phys. **64**, 1981 (1976).
[15] C. K. Jayasankar, F. S. Richardson, M. F. Reid, P. Porcher, and P. Caro, Inorg. Chim. Acta **139**, 291 (1987).
[16] G. Meyer, Prog. Solid State Chem. **14**, 141 (1982).
[17] D. R. Foster, F. S. Richardson, and R. W. Schwartz, J. Chem. Phys. **82**, 601 (1985).
[18] P. A. Tanner, Chem. Phys. Lett. **145**, 134 (1988).
[19] P. A. Tanner, J. Quagliano, and F. S. Richardson, J. Chem. Soc., Faraday Trans. **87**, 1707 (1991).
[20] P. A. Tanner, V. V. Ravi Kanth Kumar, C. K. Jayasankar, and M. F. Reid, J. Alloys Compd. **215**, 349 (1995).
[21] B. C. Tofield and H. P. Weber, Phys. Rev. B **10**, 4560 (1974).
[22] W. Stręk, Z. Mazurak, C. Szafrański, J. Hanuza, K. Hermanowicz, and B. Jezowska-Trzebiatowska, Chem. Phys. **84**, 269 (1984).
[23] A. Collombet, Y. Guyot, C. S. K. Mak, P. A. Tanner, and M.-F. Joubert, J. Lumin. **94**, 39 (2001).
[24] P. A. Tanner, Top. Curr. Chem. **241**, 167 (2004).
[25] L. Ning, P. A. Tanner, and S. Xia, Vib. Spectrosc. **31**, 51 (2003).
[26] G. P. Knudsen, Solid State Commun. **49**, 1045 (1984).
[27] G. P. Knudsen, F. W. Voss, R. Nevald, and H.-D. Amberger, in *Rare Earths in Modern Science and Technology*, edited by G. J. McCarthy, H. B. Silber, and J. J. Rhyne (Plenum, New York, 1982), Vol. 3, p. 335.
[28] M. V. Gorev, S. V. Misyul, A. F. Bovina, I. M. Iskornev, I. T. Kokov, and I. N. Flerov, J. Phys. C **19**, 2441 (1986).
[29] P. A. Tanner, C. S. K. Mak, and M. D. Faucher, J. Chem. Phys. **114**, 10860 (2001).
[30] M. D. Faucher and P. A. Tanner, Mol. Phys. **101**, 983 (2003).
[31] M. D. Faucher, P. A. Tanner, and C. S. K. Mak, J. Phys. Chem. A **108**, 5278 (2004).
[32] L. R. Morss, M. Siegel, L. Stinger, and N. Edelstein, Inorg. Chem. **9**, 1771 (1970).
[33] H.-D. Amberger, G. G. Rosenbauer, and R. D. Fischer, J. Phys. Chem. Solids **38**, 379 (1977).
[34] See EPAPS Document No. E-PRBMDO-73-013607 for the absorption and emission spectra. This document can be reached via a direct link in the online article's HTML reference section or via the EPAPS homepage (http://www.aip.org/pubservs/epaps.html).
[35] R. D. Peacock, Struct. Bonding (Berlin) **22**, 83 (1975).
[36] P. A. Tanner, C. S. K. Mak, M. D. Faucher, W. M. Kwok, D. L. Phillips, and V. Mikhailik, Phys. Rev. B **67**, 115102 (2003).
[37] P. A. Tanner, Mol. Phys. **58**, 317 (1986).
[38] H. Yersin, H. Otto, J. I. Zink, and G. Gliemann, J. Am. Chem. Soc. **102**, 951 (1980).
[39] S. L. Chodos and R. A. Satten, J. Chem. Phys. **62**, 2411 (1975).
[40] B. R. Judd, *Operator techniques in Atomic Spectroscopy* (Princeton University Press, Princeton, 1998).
[41] B. G. Wybourne, *Spectroscopic Properties of Rare Earths* (Wiley Interscience, New York, 1965).
[42] B. R. Judd, Phys. Rev. **141**, 4 (1966).
[43] K. Rajnak and B. G. Wybourne, Phys. Rev. **132**, 280 (1963).
[44] P. A. Tanner, C. S. K. Mak, W.-M. Kwok, D. L. Phillips, and M. D. Faucher, Phys. Rev. B **66**, 165203 (2002). (In Table III, the values of σ for calculations $E1$ and $E2$ should be interchanged.)
[45] M. Faucher and D. Garcia, Comptes Rendus Acad. Sci. Paris, Série II **307**, 2015 (1988).
[46] M. Faucher, D. Garcia, and P. Porcher, Comptes Rendus Acad. Sci. Paris, Série II **308**, 603 (1989).
[47] C. L. Li and M. F. Reid, Phys. Rev. B **42**, 1903 (1990).
[48] C. W. Nielson and G. F. Koster, *Spectroscopic Coefficients for the p^n, d^n, and f^n Configurations* (MIT Press, Cambridge, 1963).
[49] O. K. Moune, D. Garcia, and M. Faucher, J. Phys. Chem. Solids **52**, 513 (1991).
[50] D. Garcia and M. Faucher, *Handbook on the Physics and Chemistry of Rare Earths* edited by K. A. Gschneidner Jr. and L. Eyring (Elsevier Science, New York, 1995), Vol. 21.
[51] M. Faucher, D. Garcia, P. Caro, J. Derouet, and P. Porcher, J. Phys. (France) **50**, 219 (1989).
[52] D. Garcia and M. Faucher, J. Chem. Phys. **91**, 7461 (1989).
[53] M. D. Faucher and O. K. Moune, J. Alloys Compd. **250**, 306 (1997).
[54] R. D. Cowan, Computer program RCN31 (September 1981).
[55] D. Garcia and M. Faucher, J. Chem. Phys. **82**, 5554 (1985).
[56] C. Xueyan and L. Zundu, J. Phys.: Condens. Matter **10**, 5147 (1998).
[57] J. B. Gruber, D. S. Sardar, T. H. Allik, and B. Zandi, Opt. Mater. **27**, 351 (2004).
[58] J. B. Gruber, E. R. Menzel, and J. L. Ryan, J. Chem. Phys. **51**, 3816 (1969).
[59] M. Chertanov, O. K. Moune, B. Piriou, J. Dexpert-Ghys, M. Faucher, and M. Guittard, J. Lumin. **59**, 231 (1994).
[60] M. Faucher, D. Garcia, E. Antic-Fidancev, and M. Lemaitre-Blaise, J. Phys. Chem. Solids **50**, 1227 (1989).
[61] L. Beaury, J. Derouet, P. Porcher, P. Caro, and P. G. Feldman, J. Less-Common Met. **126**, 263 (1986).
[62] P. Caro, J. Derouet, L. Beaury, G. Teste de Sagey, J. P. Chaminade, J. Aride, and M. Pouchard, J. Chem. Phys. **74**, 2698 (1981).
[63] P. Caro, J. Derouet, L. Beaury, and E. Soulié, J. Chem. Phys. **70**,

2542 (1979).
[64] E. Antic-Fidancev, M. Lemaitre-Blaise, L. Beaury, G. Teste de Sagey, and P. Caro, J. Chem. Phys. **73**, 4613 (1980).
[65] J. B. Gruber and R. S. Satten, J. Chem. Phys. **39**, 1455 (1963).
[66] P. S. May, C. K. Jayasankar, and F. S. Richardson, Chem. Phys. **138**, 123 (1989).
[67] P. Caro, D. R. Svoronos, E. Antic, and M. Quarton, J. Chem. Phys. **66**, 5284 (1977).
[68] G. W. Burdick, C. K. Jayasankar, F. S. Richardson, and M. F. Reid, Phys. Rev. B **50**, 16309 (1994).
[69] N. C. Chang, J. Chem. Phys. **44**, 4044 (1966).
[70] O. Guillot-Noel, A. Kahn-Harari, B. Viana, D. Vivien, E. Antic-Fidancev, and P. Porcher, J. Phys.: Condens. Matter **10**, 6491 (1998).
[71] W. T. Carnall, G. L. Goodman, K. Rajnak, and R. S. Rana, Report No. ANL-88-8, Argonne National Laboratory, February, 1988 (unpublished).
[72] M. Faucher, D. Garcia, and O. K. Moune, J. Lumin. **51**, 341 (1992).